Global Biogeochemical Cycles®

RESEARCH ARTICLE
10.1029/2022GB007330

Dissolved and Particulate Barium Distributions Along the US GEOTRACES North Atlantic and East Pacific Zonal Transects (GA03 and GP16): Global Implications for the Marine Barium Cycle

Shaily Rahman[1,2,3], Alan M. Shiller[1], Robert F. Anderson[4,5], Matthew A. Charette[6], Christopher T. Hayes[1], Melissa Gilbert[1], Karen R. Grissom[1,7], Phoebe J. Lam[8], Daniel C. Ohnemus[9], Frank J. Pavia[4,5,10], Benjamin S. Twining[11], and Sebastian M. Vivancos[4,5]

[1]School of Ocean Science and Engineering, Stennis Space Center, University of Southern Mississippi, Hattiesburg, MS, USA, [2]Now at Institute of Arctic and Alpine Research (INSTAAR), University of Colorado Boulder, Boulder, CO, USA, [3]Now at Department of Geological Sciences, University of Colorado Boulder, Boulder, CO, USA, [4]Lamont-Doherty Earth Observatory of Columbia University, Palisades, NY, USA, [5]Department of Earth and Environmental Sciences, Columbia University, New York, NY, USA, [6]Department of Marine Chemistry and Geochemistry, Woods Hole Oceanographic Institution, Woods Hole, MA, USA, [7]Now at National Oceanic and Atmospheric Administration, National Weather Service, Stennis Space Center, National Data Buoy Center, Vicksburg, MS, USA, [8]Department of Ocean Sciences, University of California, Santa Cruz, Santa Cruz, CA, USA, [9]Skidaway Institute of Oceanography, University of Georgia, Savannah, GA, USA, [10]Now at Division of Geological and Planetary Sciences, California Institute of Technology, Pasadena, CA, USA, [11]Bigelow Laboratory for Ocean Sciences, East Boothbay, ME, USA

Key Points:

- Water mass mixing can account for most dissolved barium (dBa) variations in both Atlantic and Pacific transects
- Ba inputs to the ocean from broad continental shelves, ~17 Gmol year^{-1}, are substantial and may bring Ba isotope budget into mass balance
- Burial efficiencies of Ba, likely as barite, are variable ranging from 17% to 100%

Supporting Information:

Supporting Information may be found in the online version of this article.

Correspondence to:

S. Rahman,
shaily.rahman@colorado.edu

Citation:

Rahman, S., Shiller, A. M., Anderson, R. F., Charette, M. A., Hayes, C. T., Gilbert, M., et al. (2022). Dissolved and particulate barium distributions along the US GEOTRACES North Atlantic and East Pacific Zonal Transects (GA03 and GP16): Global implications for the marine barium cycle. *Global Biogeochemical Cycles*, *36*, e2022GB007330. https://doi.org/10.1029/2022GB007330

Received 21 JAN 2022
Accepted 19 MAY 2022

Abstract Processes controlling dissolved barium (dBa) were investigated along the GEOTRACES GA03 North Atlantic and GP16 Eastern Tropical Pacific transects, which traversed similar physical and biogeochemical provinces. Dissolved Ba concentrations are lowest in surface waters (~35–50 nmol kg^{-1}) and increase to 70–80 and 140–150 nmol kg^{-1} in deep waters of the Atlantic and Pacific transects, respectively. Using water mass mixing models, we estimate conservative mixing that accounts for most of dBa variability in both transects. To examine nonconservative processes, particulate excess Ba (pBa_{xs}) formation and dissolution rates were tracked by normalizing particulate excess ^{230}Th activities. Th-normalized pBa_{xs} fluxes, with barite as the likely phase, have subsurface maxima in the top 1,000 m (~100–200 μmol m^{-2} year^{-1} average) in both basins. Barite precipitation depletes dBa within oxygen minimum zones from concentrations predicted by water mass mixing, whereas inputs from continental margins, particle dissolution in the water column, and benthic diffusive flux raise dBa above predications. Average pBa_{xs} burial efficiencies along GA03 and GP16 are ~37% and 17%–100%, respectively, and do not seem to be predicated on barite saturation indices in the overlying water column. Using published values, we reevaluate the global freshwater dBa river input as 6.6 ± 3.9 Gmol year^{-1}. Estuarine mixing processes may add another 3–13 Gmol year^{-1}. Dissolved Ba inputs from broad shallow continental margins, previously unaccounted for in global marine summaries, are substantial (~17 Gmol year^{-1}), exceeding terrestrial freshwater inputs. Revising river and shelf dBa inputs may help bring the marine Ba isotope budget more into balance.

1. Introduction

Oceanic dissolved and particulate barium have been proposed as useful tracers of various processes, such as ocean circulation (Bacon & Edmond, 1972; Chan et al., 1976; Jeandel et al., 1996), water column organic carbon respiration (Dehairs et al., 1997; Jacquet et al., 2011; Lemaitre et al., 2018; Shopova et al., 1995), seawater composition (Geyman et al., 2019; LaVigne et al., 2011; Rubin et al., 2003), shelf inputs (Ho, Shim, et al., 2019; Roeske, Bauch, et al., 2012; Roeske, Loeff, et al., 2012), including submarine groundwater discharge (SGD; Shaw et al., 1998), and river inputs (Guay & Falkner, 1997; McCulloch et al., 2003). Ratios of Ba to Ca preserved in foraminiferal tests and deep-sea corals have been used to reconstruct continental inputs of Ba to the ocean and its deep-sea concentrations through time, which can be used as an analog for other nutrient distributions (Hall & Chan, 2004; LaVigne et al., 2011; McCulloch et al., 2003). The sedimentary barium record has been probed as a potential proxy for primary productivity and export production (Collier & Edmond, 1984; Dehairs et al., 1980;

Table 1
Summary of dBa Fluxes Into and Out of the Ocean in Prior Summaries of the Marine Ba Cycle

	Paytan and Kastner (1996)[a] and Dickens et al. (2003)[b]	Reevaluated fluxes
Inputs		
Rivers (dBa)	14.7 Gmol/yr[a,b,h]	7 ± 4 Gmol/yr[c,d]
Estuarine processes	n.d.	3–13 Gmol/yr[e]
Hydrothermal vents (dBa)	3.4 Gmol/yr[a]	<2–3 Gmol/yr[a,f]
Eolian	n.d.	n.d.
Terrestrial SGD	0 Gmol/yr[a,b]	0.4–3.6 Gmol/yr[d]
Total (terrestrial + marine) SGD	0 Gmol/yr[a,b]	17 Gmol/yr[c]
Total inputs	18.1[i]	29–44[i]
Outputs		
Open ocean pBa_{xs} burial (>1,000 m)	n.d.	>19 ± 10 Gmol/yr[g]
Coastal ocean burial (<1,000 m)	n.d.	<8[j]
Total burial	18[a,b]	26–27
Residence time	~8.5 kyr[a,b]	3.5–5 kyr[c]

Note. A budget with reevaluated flux estimates is presented for comparison with associated changes in residence time (n.d. = not determined).

[a]Paytan and Kastner (1996). [b]Dickens et al. (2003). [c]This study. [d]Mayfield et al. (2021). [e]Bridgestock et al. (2021). [f]Hsieh et al. (2020). [g]Hayes et al. (2021). [h]This estimate accounts for freshwater dissolved barium (dBa) input and dBa released from desorption or dissolution from suspended particulate matter during estuarine mixing. [i]Sum of rivers, hydrothermal vents, and total shelf sources. [j]Difference between total pBa_{xs} burial and open ocean pBa_{xs} burial.

Dymond & Collier, 1996; Eagle et al., 2003; Francois et al., 1995), paleoproductivity (Dymond & Collier, 1996; Hernandez-Sanchez et al., 2011; Klump et al., 2001; McManus et al., 1999; Paytan et al., 1996; Paytan & Griffith, 2007; Schoepfer et al., 2015; Thomas et al., 2011), and paleoalkalinity (Lea, 1993; Lea & Boyle, 1989; Rubin et al., 2003) though it may have limited utility as an alkalinity tracer (Rubin et al., 2003; Thomas et al., 2011). Despite its promise, there are major gaps in our knowledge of the modern ocean geochemical cycle of Ba, which leads to uncertainty in its use as a proxy.

The distribution of dissolved Ba (dBa) is assumed to be controlled by the formation of barite ($BaSO_{4(s)}$) in the upper ocean, large-scale ocean circulation, and barite dissolution as it sinks through the water column and in sediment after deposition (Dickens et al., 2003; Hsieh & Henderson, 2017; Paytan et al., 1996; Wolgemuth & Broecker, 1970). Water column dBa profiles are typical of bio-intermediate elements: low (but not depleted) concentrations in the upper ocean, which increase both with depth and age as deep water masses, move from the Atlantic Ocean to the Pacific. Despite barite being undersaturated throughout most of the global oceans (Church & Wolgemuth, 1972; Monnin & Cividini, 2006; Rushdi et al., 2000), authigenic barite, typically assumed to be the equivalent of empirically derived excess particulate Ba (pBa_{xs}, i.e., particulate Ba in excess of lithogenic particulate barium), appears to form in the upper few hundred meters of the ocean in supersaturated microenvironments created during POC (particulate organic carbon) respiration within sinking particulate matter aggregates (Cardinal et al., 2005; Collier & Edmond, 1984; Dehairs et al., 1980; Dymond & Collier, 1996; Shopova et al., 1995). Some regional and global studies conclude that dBa behaves nonconservatively in intermediate and deep waters as pBa_{xs} dissolves upon sinking (Hsieh & Henderson, 2017; Le Roy et al., 2018; Paytan et al., 1996), whereas others conclude that dBa demonstrates conservative behavior in waters below 2,000 m (Bates et al., 2017; Geyman et al., 2019). The potential for multiple processes to affect barium makes the interpretation of its distribution challenging.

There is considerable uncertainty in estimates of dBa flux into and out of the global ocean (Table 1). In an often-used model of the marine Ba cycle, the major vector of dBa flux to the ocean is assumed to be via rivers, which delivers ~15 Gmol of Ba annually (Dickens et al., 2003; Paytan et al., 1996). The riverine flux has been based on dBa concentrations in the Zaire River or in a set of unnamed North American rivers (Edmond et al., 1978; Livingstone, 1963; Paytan et al., 1996; Wolgemuth & Broecker, 1970). In this model, dBa distributions with

depth, between the surface and deep ocean, are controlled by the formation and dissolution of a particulate phase, barite (i.e., Dickens et al., 2003). Of the ~103 Gmol year^{-1} of particulate Ba that is estimated to form in the upper ocean, only ~18 Gmol year^{-1} is removed via sediment burial (Dickens et al., 2003; Paytan et al., 1996). The estimated remainder, ~85 Gmol year^{-1} (~86%), dissolves upon sinking through the water column or in sediment post-deposition (Dickens et al., 2003; Paytan et al., 1996). Hydrothermal vents supply another 3.4 Gmol year^{-1} (Dickens et al., 2003). With an estimated inventory of ~150 Tmol, the residence time of dBa in the ocean is ~8.5 ky (Dickens et al., 2003; Paytan et al., 1996). Considering present-day approximations, the estimated stable Ba isotopic compositions of sources and sinks of Ba imply an imbalance in the conceptual marine budget, where purported sources are significantly enriched in the heavier stable isotope than major sinks (Bridgestock et al., 2018; Cao et al., 2016, 2020; Horner & Crockford, 2021; Horner et al., 2021; Hsieh & Henderson, 2017; Mayfield et al., 2021). Evidence suggests that there should be one or more sources with a light isotopic signature to balance the budget, unaccounted sinks with a heavy isotopic signature, or a combination of both.

There are several large-scale transects of dBa in the Atlantic, Southern, and now Arctic Oceans (Chan et al., 1976, 1977; Haine et al., 2015; Jacquet et al., 2007; Jeandel et al., 1996; Le Roy et al., 2018; Monnin & Cividini, 2006; Thomas et al., 2011; van Beek et al., 2007; Whitmore et al., 2021). The data on dBa distributions in the Pacific (Bacon & Edmond, 1972; Chan et al., 1976; Wolgemuth, 1970) and Indian Ocean are sparse (Jeandel et al., 1996; Li et al., 1973; Monnin et al., 1999) with oceanographic sections limited mainly to those from the GEOSECS cruises several decades ago. Here, we investigate dissolved and particulate Ba behavior along the GEOTRACES GA03 North Atlantic transect and GP16 Southeast Pacific transect, which occupied similar biogeochemical ocean provinces. Both sections sampled eastern margin upwelling regions, oxygen minimum zones (OMZs), hydrothermal vent inputs, and subtropical gyres, but occupied different stages of meridional overturning circulation with different water mass age distributions (e.g., Khatiwala et al., 2012). In this study, we examine regions of nonconservative dBa behavior along the two transects. Part of our aim is to use various methodologies, for example, water mass deconvolutions (Jenkins, Lott, et al., 2015; Peters et al., 2018), to probe for nonconservative behavior as none of these methods on their own are perfect. We report excess ^{230}Th-normalized pBa_{xs} flux and accumulation in both basins, investigating barite dissolution and burial efficiencies. Finally, we generally predict zones of expected nonconservative dBa behavior in the global ocean and reassess regional and global conceptual marine Ba models.

2. Materials and Methods

2.1. Oceanographic Sampling

In 2010 and 2011, the US GEOTRACES cruise GA03 surveyed the North Atlantic in two sections aboard the R/V Knorr. Twelve stations were sampled along a meridional section KN199-04 from Lisbon, Portugal to Cape Verde in 15 October to 4 November 2010; whereas 22 stations were sampled in 6 November to 11 December 2011, along the roughly zonal transect KN204-01 from Cape Cod, USA, to Praia, Cape Verde (Figure 1). Dissolved samples at each station were collected using 12-L Teflon-coated GO-FLO (General Oceanics) bottles mounted on a trace metal clean GEOTRACES rosette (Cutter & Bruland, 2012; Hatta et al., 2015; Measures et al., 2008). Approximately 10–15 samples were collected between 0 and 1,000 m and 10–15 samples collected in the remainder of the water column. Samples were filtered through 0.2 µm Pall AcroPak™ Supor® capsules and collected in pre-cleaned (1.2 M reagent grade HCl, heated for a minimum of 8 hr and rinsed with ultrapure water) 125-ml high-density polyethylene (HDPE) bottles. Samples were acidified onboard to a pH of ~1.7 and stored at room temperature during transport back to the laboratory. Surface water samples were also collected using an underway towed fish and filtered through a 0.45-µm Osmonics and a 0.2-µm polycarbonate track-etched cartridge filter (Bruland et al., 2005). Additional surface water samples were taken after the KN199-04 cruise along a cruise track from Cape Verde to Charleston, USA (KN199-05).

In 2013 (25 October to 20 December), aboard the R/V Thomas G. Thompson (TN303, GP16), the US GEOTRACES sampled 35 stations in the eastern Pacific Ocean from Manta, Ecuador to Papeete, French Polynesia. Sampling included 4 shelf stations, 13 shallow stations (~1,000 m depth), and 17 full depth stations. At full depth stations, typically ~20 samples were collected in the upper 0–1,000 m and another ~20 collected in the remainder of the water column. Dissolved samples were collected for trace elements at cast stations as well as underway surface towed-fish samples (3.5 m) (Bruland et al., 2005). Cast station samples were collected using trace metal clean techniques, filtered through 0.2 µm Pall AcroPak™ Supor® capsules, and collected

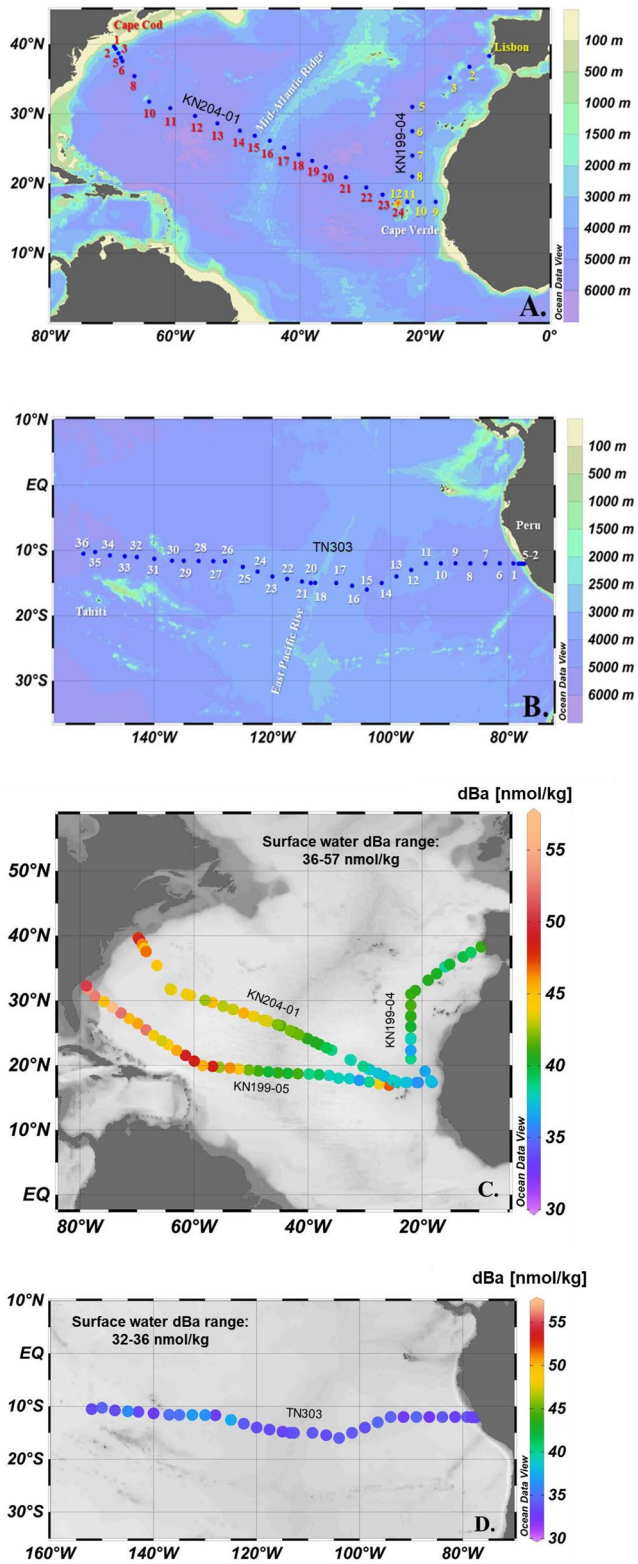

Figure 1. (a). U.S. GEOTRACES GA03 KN199-04 and KN204 cruise tracks in the North Atlantic. All KN199-04 meridional transect stations are labeled in yellow from Lisbon to Cape Verde, whereas KN204 zonal transect stations from Cape Cod, MA to Cape Verde, are labeled in red. The crossover station, KN199 St. 12 and KN204 St.24, is indicated by the orange dot. (b) U.S. GEOTRACES GP16 East Pacific Zonal Transect cruise track from Peru to Tahiti. (c) Station numbers are shown in white. Surface water dissolved Ba (dBa) concentrations from KN199-04, KN199-05, and KN204 in the North Atlantic. (d) Surface water dBa concentrations from GP16 in the East Pacific.

in pre-cleaned 125-ml HDPE bottles (Cutter & Bruland, 2012; Measures et al., 2008). Underway towed-fish samples were filtered through a 0.45-µm Osmonics and a 0.2-µm polycarbonate cartridge (Bruland et al., 2005). These samples were stored at room temperature and shipped to the laboratory before acidification with 500 µl of 6 N ultrapure HCl (Fisher, Optima) to a pH of ∼1.8. Along GP16, surface sediments were also collected using a mono-corer attached to a CTD rosette (German, 2017). Cores were stored upright and refrigerated before return to Lamont-Doherty Earth Observatory (LDEO), where each mono-core was split and analyzed nondestructively. One half core was then archived at LDEO and the other half made available for sampling. The upper 1 cm of mono-cores was analyzed. The cores were not explicitly dated. The core tops likely represent Holocene material but could contain older sediments. Particulate trace element samples on both GA03 and GP16 were collected by in-situ pumping and on GP16, additional particle samples were collected by GO-FLO filtration. Particulate sampling is described further in Section 2.3.

Standard hydrographic analyses (salinity, dissolved oxygen, and micromolar nutrients) are conducted for all GEOTRACES cruises. Data from the North Atlantic cruises can be found through the Biological and Chemical Oceanography Data Management Office (BCO-DMO) data repository (https://www.bco-dmo.org/project/2066). Hydrographic data from GP16 can also be found in the BCO-DMO database (https://www.bco-dmo.org/project/499723). The data are also available through the GEOTRACES Data Assembly Center (www.bodc.ac.uk/geotraces).

2.2. Dissolved Barium Analysis

Dissolved Ba was determined by isotope dilution with subsequent analysis with a sector field inductively coupled plasma mass spectrometer (SF-ICP-MS, ThermoFisher Element 2) (Jacquet et al., 2007; Shim et al., 2012). Briefly, the acidified seawater sample was diluted approximately 30-fold by adding 50 µL of sample into 1.5 mL of ultra-pure distilled water. A 25 µl ^{135}Ba-spike solution, prepared from solid $BaCO_3$ powder provided by Oak Ridge National Laboratory (93.8% ^{135}Ba; ∼180 nmol L^{-1}), was added to the diluted sample. Pipettes were calibrated by mass after each analytical run to determine exact sample and spike additions. Samples were introduced to the SF-ICP-MS through a PFA microflow nebulizer (Elemental Scientific, Inc.) and a PFA PURECHAMBER™ Spray chamber (Elemental Scientific, Inc.). Samples were analyzed by SF-ICP-MS in low resolution for both ^{135}Ba and ^{138}Ba. Data were verified by the analysis of US GEOTRACES intercalibration surface (GS) and deep water (GD) samples at the beginning and end of each analytical run (Atlantic: GS 43.0 ± 1.1 [n = 20], GD 52.7 ± 0.5 [n = 20]; Pacific: GS 43.7 ± 1.0 [n = 15], GD 54.3 ± 1.5 [n = 15]; nmol kg-SW^{-1}) (Shiller, 2016a, 2016b). Samples were bracketed by a blank and a ^{135}Ba spiked solution every 10 samples. Blank counts are monitored and subtracted out of the data. Intercalibration and in-house standards suggest a precision of 2%–3% and a detection limit of 0.7 nmol kg^{-1} (Shiller, 2016a, 2016b).

2.3. Particulate Phase Trace Element Analysis

Filtered particle collection and digestion procedures have been described previously (Ohnemus et al., 2014, 2017, 2019; Ohnemus & Lam, 2015). Briefly, following protocols in compliance with GEOTRACES methods for collecting samples using in situ pumps (GA03; Lam, 2018) and GO-FLO bottles (GP16; Sherrell et al., 2016), particles were collected on acid-cleaned polyethersulfone (Supor®) filters. With in situ pumps, two particle size classes were collected: a small-size class (0.8–51 µm) and a large-size class (>51 µm) on polyester mesh filters that were rinsed with filtered seawater onto a 0.8 µm Supor® filter. For pump samples, particulate Ba (pBa) was the sum of the small- and large-size fraction. Only one size class (>0.45 µm) was collected via filtration from GO-FLO samples. A mixture of 4M each HCl, HF, and HNO_3 acids was used to completely digest samples collected by GO-FLO and in-situ pumps. Filters collected using in situ pumps also included a pre-digestion step using piranha reagent, a mixture of sulfuric acid and peroxide, that completely dissolved the Supor® filter prior to the main particle digestion (Ohnemus & Lam, 2015). Digested samples were dried and brought up in dilute HNO_3 for analysis via a Thermo Element 2 HR-ICP-MS. Interlaboratory comparisons of these different digestion procedures demonstrate that they yield similar results (Ohnemus et al., 2014).

Particulate trace element concentrations determined in samples collected via in situ pumps were compared to concentrations determined in GO-FLO samples (Twining et al., 2015), so we assumed minor differences between the collection methods on particulate Ba concentrations. While GA03 pBa results were oceanographically

consistent, irregularities in GP16 in-situ pump pBa profiles digested by the piranha method suggest that there may have been some interference between sulfuric acid and pBa (as $BaSO_4$) dissolution in some instances, and we no longer recommend this digestion method for pBa. For this reason, GP16 in-situ pump pBa profiles are not presented here. Particulate Ba from GA03 is from pump samples, and pBa from GP16 is from bottle samples. Several GP16 pump pBa profiles (stations 1, 18, and 36, spanning the beginning, middle, and end of the transect) did not have piranha digestion issues, allowing a direct comparison of pump and bottle sampling methods. This comparison suggests that bottle pBa was typically 23% ± 4% higher than pBa concentrations from pumps, at least at these three stations on GP16 (Figure S2a in Supporting Information S1). This is a caveat that should be kept in mind since we did not make any further assumptions of which the collection method (pump vs. bottle) better represents actual pBa concentrations, nor were corrections applied. The higher pBa concentrations in bottle samples are likely from the <0.8 μm size class, which was not sampled via in situ pumps. All data are publicly available through the U.S. Biological and Chemical Oceanography Data Management Office (www.bco-dmo.org) and GEOTRACES Data Assembly Center (www.bodc.ac.uk/geotraces). The GP16 pBa data have been previously published (Ohnemus et al., 2019).

2.4. Calculation of Excess Particulate Barium and Barite Solubility

Water column excess particulate barium, pBa_{xs}, is empirically derived by subtracting lithogenic Ba from total particulate Ba (pBa). Ratios of Ba:Al (e.g., Dehairs et al., 1997, 2008; Lemaitre et al., 2018) or Ba:^{232}Th (e.g., van Beek et al., 2007) in the upper continental crust, $(Ba/Al)_{UCC}$ and $(Ba/^{232}Th)_{UCC}$, respectively, have been used to estimate lithogenic Ba. Here, we use particulate Al, pAl, in the water column to correct for the lithogenic Ba fraction:

$$pBa_{xs} = pBa - \text{lithogenic Ba} \quad (1)$$

$$pBa_{xs} = pBa - \left(\frac{Ba}{Al}\right)_{UCC} (pAl) \quad (2)$$

Estimated $(Ba/Al)_{UCC}$ ranges from 0.0013 to 0.0029 mol:mol (Condie, 1993; D. M. Shaw et al., 1976, 1967; Gao et al., 1998; Rudnick & Gao, 2014; Taylor & Mclennan, 1995) and the section plots were made using the recommended Ba:Al value, $(Ba/Al)_{UCC} = 0.0015$ in a recent compilation of upper continental crustal compositions (Rudnick & Gao, 2014). Barite solubility and dissociation constants were calculated from temperature, pressure, salinity, dBa molality, and sulfate molality according to Pitzer's ion interaction model equations (Rushdi et al., 2000) for GA03 and GP16.

2.5. Excess ^{230}Th-Based Particulate Ba Flux

Particulate excess Ba fluxes were calculated using measured excess ^{230}Th ($p^{230}Th_{xs}$) activities on 0.8–0.51 μm pumped particles collected in GA03 (Hayes, Black, et al., 2018) and GP16 (Anderson et al., 2017; Pavia et al., 2018, 2019). The methodology for determining sinking particle fluxes using this radionuclide has previously been described in detail (Anderson et a l., 2016; Hayes, Black, et al., 2018; Hirose, 2006; Pavia et al., 2019) and only a summary is provided here. The production of dissolved ^{230}Th ($d^{230}Th$, $t_{1/2} = 75{,}600$ years) in the ocean is set by the radioactive decay of dissolved ^{234}U, which varies with salinity. ^{234}U activity was calculated from salinity and the global seawater ^{234}U:^{238}U activity ratio of 1.1468 (Andersen et al., 2010; Owens et al., 2011). The disequilibrium between predicted dissolved ^{230}Th and actual ^{230}Th activities is generated by the particle reactivity of ^{230}Th: most of the dissolved ^{230}Th produced in the water column is rapidly removed from the dissolved phase by sinking particles (Moore & Sackett, 1964). The ^{230}Th activity on particles ($^{230}Th_{xs}$) and ratios of pBa_{xs}:$^{230}Th_{xs}$ were used to calculate $^{230}Th_{xs}$-normalized (hereafter abbreviated as Th-normalized) pBa_{xs} particulate fluxes (see Text S2 in Supporting Information S1 for further details). At GA03, both small and large particle sizes were characterized for pBa_{xs} and $^{230}Th_{xs}$. The sensitivity of pBa_{xs} sinking flux estimates to particle size class was determined by comparing pBa_{xs}:$^{230}Th_{xs}$ ratios in the small-size fraction (SSF; 0.8–0.51 μm) to pBa_{xs}:$^{230}Th_{xs}$ ratios in the large-size fraction (LSF) (>0.51 μm; Figure S2b in Supporting Information S1). The sensitivity of particle flux to particle size in GP16 was assumed to be similar to the sensitivity in GA03.

2.6. Estimating Nonconservative Dissolved Ba

Conservative [Ba] distributions were derived using prior water mass deconvolutions based on Optimum Multi-Parameter Analysis (OMPA) of tracer distributions in the North Atlantic GA03 section (Jenkins, Smethie, et al., 2015) and South Pacific GP16 section (Peters et al., 2018) paired with dBa. These deconvolutions are not perfect and are just one of our tools for probing nonconservative behavior. End-member dBa for each GA03 water mass was chosen from existing GEOSECS (https://odv.awi.de/data/ocean/geosecs/) or GEOTRACES stations (Table S1 in Supporting Information S1) as geographically close to stations with water mass properties chosen by Jenkins, Lott, et al. (2015) and Jenkins, Smethie, et al. (2015) (Charette et al., 2015; Fiz et al., 2020; Fogelqvist et al., 2003; García-Ibáñez et al., 2018; Jenkins, Smethie, et al., 2015; Le Roy et al., 2018; Sutton et al., 2018; Tanhua et al., 2005). Most GP16 dBa water mass end-members were defined in GEOSECS stations (Table S2 in Supporting Information S1) as close as possible to the geographical locations that Peters et al. (2018) used for their OMPA. We also followed the end-member labeling scheme chosen by Jenkins, Lott, et al. (2015) and Jenkins, Smethie, et al. (2015) and Peters et al. (2018) realizing that their choice of location of a given water mass type may differ from textbook definitions. The OMP Analyses for each transect have already been discussed in detail (Jenkins, Smethie, et al., 2015; Peters et al., 2018). Errors, or deviation from assumed water mass conservation, in the OMP analysis for the thermocline of the GA03 and GP16 were significant enough (10%–35%) (Jenkins, Smethie, et al., 2015; Peters et al., 2018); and the dBa end-member differences are small enough between those water masses (i.e., ~3 nmol kg^{-1} difference), that $[Ba]_{nc}$ was not determined in those regions (Supporting Information). "Conservative" ($[Ba]_c$) and "nonconservative" Ba ($[Ba]_{nc}$) contributions to measured dBa ($[Ba]_{meas}$) were derived for depths below the thermocline:

$$[Ba]_c = \sum_{i=1}^{n} [[Ba]_i \times \text{fraction}_i] \quad (3)$$

$$[Ba]_{nc} = [Ba]_{meas} - [Ba]_c \quad (4)$$

where $[Ba]_i$ denotes the estimated end-member dBa in water mass i, and fraction_i is the OMPA-derived percent contribution of end-member water mass i for each sample where data are available. The depths at which the water mass OMPA were conducted were not the same depths at which dBa samples were collected. Therefore, polynomial trend lines were fit ($r^2 > 0.93$) to derived $[Ba]_c$ OMPA depth profiles at each station from which a conservative [Ba] value was interpolated for all depths sampled in the GA03 and GP16 transects. Conservative [Ba] was derived several ways in different scenarios (Supporting Information) using extreme and average end-member concentrations with details given in the Supporting Information.

2.7. Defining Section-Specific Dissolved Ba, Ra, and Si Relationships

Strong linear empirical relationships have been observed for Ba and Si, Ba and Ra, and Si and Ra throughout the global ocean (Bishop, 1988; Chan et al., 1976, 1977; Li et al., 1973). Section-specific element-element relationships were defined and used rather than global ones. We used a previously defined tracer, Ba* (Horner et al., 2015), and defined two additional tracers, Ba^{**}_{226Ra} and Si^{**}_{226Ra}, based on element-^{226}Ra correlations. Ba* is derived by the difference between measured dBa and predicted dBa based on the correlation between dBa and dissolved Si (dSi) and has been employed in other ocean basins (e.g., Bates et al., 2017; Horner et al., 2015). We define Ba^{**}_{226Ra} as the difference between measured dBa and predicted dBa based on the correlation between dBa and dissolved ^{226}Ra (d^{226}Ra). A similar relationship was derived and used to probe dBa and ^{226}Ra relationships in the subpolar North Atlantic (Le Roy et al., 2018), where nonconservative behavior was also investigated. Tracer Si^{**}_{226Ra} is derived by the difference between measured dSi from predicted dSi based on the correlation between dSi and d^{226}Ra. The d^{226}Ra results from the North Atlantic (Charette & Morris, 2015) and East Pacific (Charette & Moore, 2016) have previously been described in detail (Charette et al., 2015; Henderson et al., 2013; Kipp et al., 2018; Sanial et al., 2018).

Correlation plots (Model II geometric mean regression) in GA03 and GP16 were constructed using colocated dSi and dBa to define tracer Ba*. Dissolved ^{226}Ra measurements were taken at the same stations as dSi and dBa but at different depths. Therefore, polynomial trend lines were fit ($r^2 > 0.93$) to dBa and dSi with depth, and a [Ba] and [Si] value was interpolated for all depths sampled for d^{226}Ra for both transects.

3. Results and Discussion

3.1. Distribution of Dissolved Ba, Si, and Ra and Hydrographic Settings

Oxygen, apparent oxygen utilization (AOU), salinity, temperature, nutrient, and radiogenic isotope (e.g., ^{226}Ra, ^{228}Ra, and ^{3}He) distributions of these transects have previously been described in detail (Charette et al., 2015; Jenkins, Lott, et al., 2015; Kipp et al., 2018; Peters et al., 2018; Sanial et al., 2018). Several of these distributions are presented in the Supporting Information (Figures S1 and S4 in Supporting Information S1). Several common dominant features between the GA03 and GP16 transects are primary production driven by intense upwelling along the eastern margin (Mauritanian upwelling and Peruvian upwelling zones), similar rates of net primary production (Black et al., 2018; Buesseler & Boyd, 2009; Lovecchio et al., 2017), OMZs extending westward from the upwelling zones resulting from organic carbon remineralization, and hydrothermal vent inputs (Mid-Atlantic Ridge [MAR] and East Pacific Rise [EPR]). Some differences between the two transects include higher dust deposition fluxes (Kadko et al., 2020; Mahowald et al., 2005; Measures et al., 2015; Shelley et al., 2015), a less extensive OMZ (Figure S1 in Supporting Information S1), and higher minimum O_2 values in GA03 than in GP16. The core of the OMZ ([O_2] <100 μmol kg^{-1}) in the GA03 is around 400 m depth near Cape Verde, whereas the GP16 OMZ is more intense and widespread with <100 μmol kg^{-1} [O_2] waters extending from 100–200 to 2,000 m depth near Peru and almost reaching Tahiti west of the East EPR (Figure S1 in Supporting Information S1). Driven by upwelling, slow circulation, and near-complete C_{org} respiration (Buesseler et al., 2020; Pavia et al., 2019; Peters et al., 2018), AOU in the GP16 OMZ can be >275 μmol kg^{-1}, whereas it does not exceed ∼250 μmol kg^{-1} in the GA03. Mean water mass ages at >1,500 m depth in GA03 are relatively young (<400 years) and increase to ∼1,000 years in GP16 (Khatiwala et al., 2012).

The shapes of the depth profiles of dBa in both ocean basins are typical of a biointermediate element. The dBa distribution in the central basin of the North Atlantic transect (Figure 2a) largely reflects the influence of North Atlantic sub-polar waters with low [Ba] (38–53 nmol kg^{-1}), low [Si], and low ^{226}Ra mixing with Southern Ocean sourced waters with relatively higher [Ba] (60–111 nmol kg^{-1}), [Si], and ^{226}Ra (Le Roy et al., 2018; Sutton et al., 2018). Our results for dBa in the northeast end of the GA03 are in general agreement with results presented in Le Roy et al. (2018) from GA01 (Figure S3a in Supporting Information S1). In GA03, concentrations in surface waters are ∼38–50 nmol kg^{-1} and reach 70–86 nmol kg^{-1} in deep waters. The MAR bisects the GA03 transect with the ridge itself at Stn KN204: 16, the western basin containing stations KN204: 1–15, and the remainder of the stations (KN204: 17–24 plus all KN199 stations) in the eastern basin. Surface water dBa increases from ∼38 nmol kg^{-1} near Cape Verde in the eastern basin to 50 nmol kg^{-1} at the station nearest Cape Cod in the western basin (Figure 1c). The opposite trend is observed in deep waters: deep water concentrations in the eastern basin tend to be ∼10 to 15 nmol kg^{-1} higher than in the deep western basin.

In GP16, dBa is low, 30–35 nmol kg^{-1}, in the top 200 m, and increases to a maximum of ∼125–140 nmol kg^{-1} between 2,500 and 3,000 m and then decreases by 10–15 nmol kg^{-1} at depth (Figure 2b). Much of the GP16 hydrography is bisected by the EPR (Station 18). We refer to those stations east of the EPR (stations 1–17) as being in the eastern GP16 basin, and the stations west of the EPR (Stations 20–36) as being in the western GP16 basin. Southward flowing Pacific Deep Water (PDW) with high end-member values of dBa (151–156 nmol kg^{-1}), Si, and ^{226}Ra makes up most of the water mass below 1,200 m in the eastern basin where dBa reaches 135–140 nmol kg^{-1}. Antarctic Bottom Water (AABW), Lower Circumpolar Deep Water, and Upper Circumpolar Deep Water, with intermediate concentrations of Ba (83–96 nmol kg^{-1}), Si, and ^{226}Ra dominate the deep and bottom waters west of the EPR, where dBa concentrations typically do not exceed 130 nmol kg^{-1} with a relatively low [Ba] zone of ∼125 nmol kg^{-1} in the deepest waters of the westernmost stations (Stations 33–36). Intermediate waters between 500 and 1,200 m are mainly composed of Equatorial Pacific Intermediate Water and Antarctic Intermediate Water, which have lower Ba (50–57 nmol kg^{-1}), Si, and ^{226}Ra than deeper water masses. Results are consistent with GEOSECS stations from the eastern North Atlantic and South Pacific as well as other parts of the global ocean (e.g., Bates et al., 2017; Chan et al., 1976, 1977; Horner et al., 2015; Jeandel et al., 1996; Le Roy et al., 2018).

3.2. Distribution of Excess Particulate Ba

Several possibilities exist for the types of solid phases with which pBa is associated along both transects. We examined the behavior of pBa_{xs}, that is, the non-terrigenous portion likely to impact conservative dBa

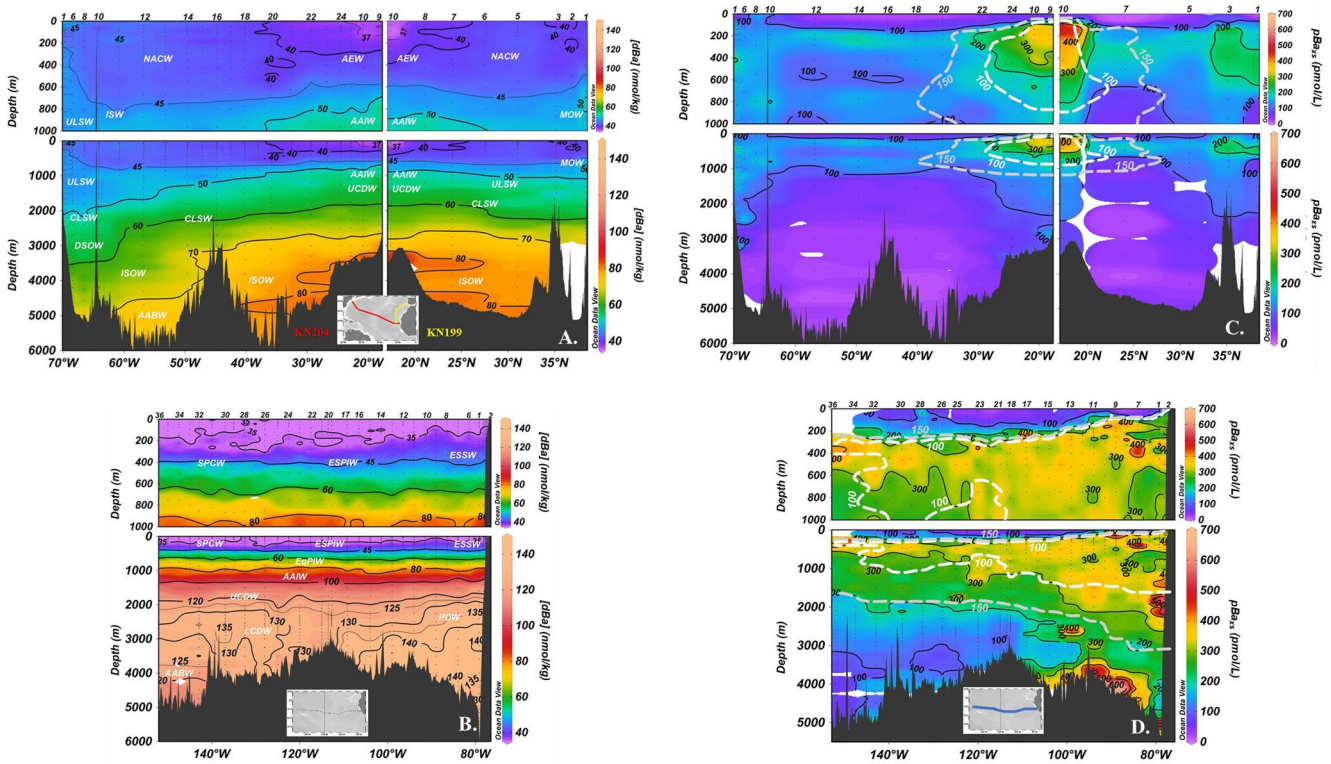

Figure 2. North Atlantic Zonal Transect (a) dBa and (c) pBa$_{xs}$ distributions. Distributions of (b) dBa and (d) pBa$_{xs}$ in the East Pacific Zonal Transect. White- and gray-dashed lines show the 100 and 150 μmol kg^{-1} O_2 contours, respectively. In these and the following figures, see Jenkins, Lott, et al. (2015) and Jenkins, Smethie, et al. (2015) (AEW-Atlantic Equatorial Water; NACW-North Atlantic Central Water; SACW-South Atlantic Central Water; AABW-Antarctic Bottom Water; DSOW-Denmark Strait Overflow Water; ISOW-Iceland-Scotland Overflow Water; CLSW-Classical Labrador Sea Water; MOW-Mediterranean Overflow Water; ULSW-Upper Labrador Sea Water; UCDW-Upper Circumpolar Deep Water; AAIW-Antarctic Intermediate Water; ISW_Irminger Sea Water) and Peters et al. (2018) (ESSW-Equatorial Subsurface Water; ESPIW-Easter South Pacific Intermediate Water; SPCW-South Pacific Central Water; AAIW-Antarctic Intermediate Water; EqPIW-Equatorial Pacific Intermediate Water; UCDW-Upper Circumpolar Deep Water; PDW-Pacific Deep Water LCDW-Lower Circumpolar Deep Water; AABW-Antarctic Bottom Water) for the definitions of the abbreviated water mass labels.

distributions in the ocean. The first region of high pBa$_{xs}$ was in the southeast portion of GA03 with concentrations reaching >400 pmol L^{-1} (a seawater density of 1.025 is used for converting concentrations per kilogram to concentration per L) around 200 m in the OMZ (Figure 2c). Below the OMZ, pBa$_{xs}$ remained high, with concentrations of ∼100 pmol L^{-1} near the sediment-water interface at ∼3,000–3,500 m. Another region of high pBa$_{xs}$ was in the northeast basin (KN199 stations 1–3) at water depths <600 m. The third region of high pBa$_{xs}$ was along the continental margin in the northwest basin, where high pBa$_{xs}$ (>100 pmol L^{-1}) was found in samples deeper than 3,000 m at stations west of Bermuda. This region in the northeast basin (KN204 stations 1–8) is characterized by high-suspended sediment concentration and significant lithogenic inputs (Lam et al., 2015; Ohnemus & Lam, 2015).

In the East Pacific, a plume of high pBa$_{xs}$ (∼300 pmol L^{-1}, often higher) extended from the Peruvian margin to Tahiti (Figure 2d). The plume penetrated from the surface down to ∼2,000 m near the continental margin and narrowed to the 200–600 m depth range at station 36 near Tahiti (Figure 2d). The second region of particularly high pBa$_{xs}$ was seen in samples near the sediment-water interface east of the EPR, coincident with a zone of high dAl and an ∼600–750 m thick benthic nepheloid layers (Ho, Resing, et al., 2019; Ohnemus et al., 2018). Excess pBa >200 pmol L^{-1} was observed at all depths in the water column in the eastern basin, whereas west of the EPR, pBa$_{xs}$ was lower, typically <200 pmol L^{-1}. Similar to the North Atlantic, the surface ∼50 m layer typically had little pBa$_{xs}$, except at near-shore stations 1–5.

The lithogenic correction was <2% and <8% of the total for most GP16 and GA03 samples, respectively, resulting in a generally linear correlation between pBa$_{xs}$ and total pBa with near-zero offset (Figure S5 in Supporting Information S1). Only near the continental margins with high lithogenic pAl inputs (e.g., GA03 Station KN199-1

and GP16 Station 4), there was a substantial (>14% up to 85%) lithogenic correction (Ohnemus et al., 2018; Ohnemus & Lam, 2015). A Ba:Al correction specific to a regional lithogenic material (Rudnick & Gao, 2014) may need to be applied in those regions rather than average $(Ba/Al)_{UCC}$ (Equation 4). We further surmise lithogenic mineral dust deposition is a negligible source of pBa_{xs} in either transect: the Ba content of dust inputs in the North Atlantic (i.e., 0.0020–0.0043 mol Ba:mol Al) (Shelley et al., 2015) is lower than the average Ba content of the upper continental crust (Rudnick & Gao, 2014), and variable dissolved Ga:Al ratios along with low dissolved Al in the surface layer indicate low aeolian inputs (Ho, Resing, et al., 2019) along GP16.

Likely mechanisms for significant dBa depletion and pBa_{xs} formation in the water column are adsorption onto iron oxyhydroxides (Sternberg et al., 2005), uptake by acantharia (Bernstein & Byrne, 2004; Bernstein et al., 1987, 1998; Michaels et al., 1995), or in situ barite formation (Bishop, 1988; Dehairs et al., 1980). With respect to the first phase, Fe oxyhydroxide distributions (not shown here) in GA03 and GP16 (Lam et al., 2015, 2018) do not coincide with either pBa_{xs} distributions nor the Th-normalized pBa_{xs} flux maxima (Figures 2c, 2d and 3), except for a limited zone in <200 m near the margin (sts 1–6) of GP16 (Heller et al., 2017). Irrespective of size fraction, distributions of Fe-oxides and pBa_{xs} are poorly correlated in both GA03 and GP16 ($r^2 < 0.01$, Figures S6 and S7 in Supporting Information S1). Acantharia, a group of marine protozoa, can incorporate Ba into their skeletons, composed of celestite ($SrSO_4$), serving as a potential removal mechanism in the surface ~400 m (Bernstein et al., 1987; Michaels et al., 1995). However, the distribution of POC (not shown here) along GA03 and GP16 (Lam et al., 2015, 2018) and pBa_{xs} distributions (Figures 2c and 2d) is poorly correlated (Figures S6 and S7 in Supporting Information S1). Furthermore, Th-normalized POC maxima at GA03 (Hayes et al., 2018) and GP16 (Pavia et al., 2019) occur at depths shallower than Th-normalized pBa_{xs} flux maxima (Section 3.3, Figure 3). Given the distribution of POC and POC flux, and that most acantharian skeletons dissolve by 900 m (Bernstein et al., 1987; Michaels et al., 1995), acantharia are not likely to be quantitatively important to pBa_{xs} formation. Similarly, though the association of Ba with $CaCO_3$ and opal has been found in marine sediments (Gonneea & Paytan, 2006; Schroeder et al., 1997), these phases (Lam et al., 2015, 2018) are poorly correlated with pBa_{xs} in the water column, irrespective of size fraction, of either transect (Figures 2c and 2d, Figures S6 and S7 in Supporting Information S1). Finally, we consider in situ water column formation of barite, which has been linked to oxygen consumption and organic carbon respiration rates in the mesopelagic zone (Dehairs et al., 1980, 1997, 2008; Jacquet et al., 2008; Lemaitre et al., 2018; Planchon et al., 2012). Barite ($BaSO_4$) is theorized to form within decaying organic matter in sulfate-enriched microenvironments (Bishop, 1988; Dehairs et al., 1990; Stroobants et al., 1991). Some studies indicate that bacteria in sinking POC provide nucleation sites for barite precipitation, whereby an amorphous phosphate-rich phase initially sequesters Ba followed by sulfate substitution of phosphate groups to form $BaSO_4$ (Gonzalez-Muñoz et al., 2012; Martinez-Ruiz et al., 2019). Because the lithogenic correction was generally minor when calculating pBa_{xs} (except for margin stations where significant detrital material was found in suspension), we conclude that pBa_{xs} calculated here for GA03 and GP16 is principally barite that was formed in situ in the water column. Unless specifically stated otherwise, pBa_{xs} will be synonymous with authigenic barite in the remainder of the paper.

Water column dissolution of pBa_{xs} may be related to barite undersaturation. Water column dissolution could contribute to positive deviations of dBa from predicted conservative concentrations in both ocean basins, whereas in situ formation of pBa_{xs} may lead to negative $[Ba]_{nc}$ in the upper ocean. Barite saturation indices calculated here were consistent with prior studies of barite saturation in the world's oceans (Jeandel et al., 1996; Monnin, 1999; Monnin & Cividini, 2006; Monnin et al., 1999; Rushdi et al., 2000). At GA03, barite saturation is ~50% at 1,000 m (Figure S8 in Supporting Information S1) throughout the transect. In the eastern GA03 basin saturation increases with depth to approximately 70%, whereas it typically remains lower than 60% in the western basin. Only in the deepest samples below ~4,500 m, barite saturation is below 50%. In GP16, barite saturation reaches 100% by ~1,200 m, increases with depth to ~135% around 2,500 m, and then decreases to <100% below 4,000 m (Figure S8 in Supporting Information S1). Along with slow particle remineralization (Bates et al., 2017; Geyman et al., 2019; Hsieh & Henderson, 2017), higher dBa in the Pacific Ocean, which limits pBa_{xs} water column dissolution, may partially explain the higher pBa_{xs} found along GP16 than in GA03 (Dymond et al., 1992; Rushdi et al., 2000). Below (Section 3.3), we use particulate ^{230}Th ($p^{230}Th$) activities to track pBa_{xs} formation and dissolution rates in the water column and sediment, rates which will contribute to nonconservative dBa behavior in each ocean basin. Barite saturation indices in either basin may only partially predict pBa_{xs} distributions, and kinetics of formation and dissolution likely play a role.

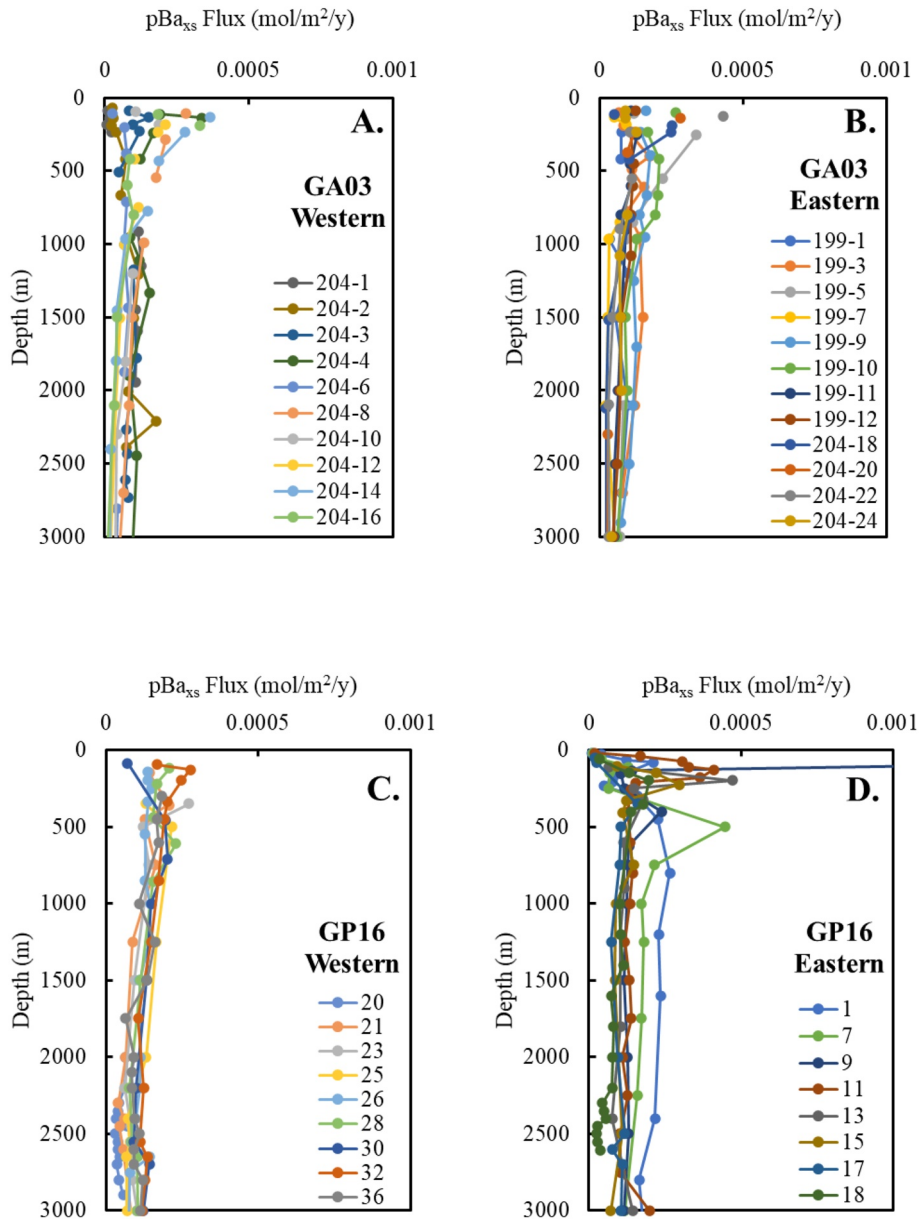

Figure 3. ^{230}Th-normalized pBa$_{xs}$ flux in the water column in the western (a) and eastern (b) basins of GA03. Corresponding ^{230}Th-normalized Ba$_{xs}$ flux at stations in the western (c) and eastern (d) basins of GP16 (the maximum flux at station 9, 0.0025 mol m^{-2} year^{-1}, is off scale).

3.3. Excess Particulate ^{230}Th-Normalized pBa$_{xs}$ Flux

The average formation and removal rates of particulate matter in the water column over timescales of several years to decades can be tracked through the disequilibrium between ^{230}Th water column activities predicted by decay of its ^{234}U parent and its measured activity on particulate matter (Bacon & Anderson, 1982; Moore & Sackett, 1964). By using the radioactive disequilibrium between ^{230}Th and ^{234}U, high spatial resolution particle flux distributions can be obtained while avoiding some of the major pitfalls of sediment traps, such as local fluid dynamics or trap geometry (e.g., Gardner et al., 1997). Particulate contents can be normalized to excess ^{230}Th (^{230}Th$_{xs}$) particulate activity to derive sinking particle flux of individual elements. This method has been applied in GA03 to determine particle fluxes of a suite of constituents (Hayes, Black, et al., 2018) and in GP16 to obtain particulate organic matter (POC) fluxes through the mesopelagic zone (Pavia et al., 2019). The flux of ^{230}Th in the water column is generally within 30% of the overlaying production rate (Costa et al., 2020). There is more of

an offset from production in areas with large lateral gradients in particulate flux, such as the West African margin, and in most of the open oceans, we expect uncertainty to be <30% (Costa et al., 2020). Here, we applied the water column disequilibrium method to pBa to track pBa_{xs} formation and dissolution rates from surface waters to ~3,000 m depth. Additionally, we use excess ^{230}Th-normalized pBa_{xs} mass accumulation rates (AR) in sediment to estimate pBa_{xs} preservation and Ba regeneration in deep waters and sediment. In GA03, particle fluxes were insensitive to particle size (Figure S2b in Supporting Information S1): Th-normalized flux estimates of pBa_{xs} in the SSF (0.8–0.51 μm) were 0.96 ± 0.07 (r^2 = 0.93) of the large-size class (>0.51 μm). We assumed that GP16 pBa_{xs} fluxes were also relatively insensitive to particle size class.

Th-normalized particulate Ba_{xs} flux was calculated at different depths in GA03 and GP16 between 0 and 3,000 m (Figure 3, Tables S4 and S5 in Supporting Information S2). In GA03, mesopelagic zone maxima in pBa_{xs} fluxes were typically observed between 80 and 150 m (71–364 μmol m^{-2} $year^{-1}$ and 86–428 μmol m^{-2} $year^{-1}$ in the western and eastern basins, respectively, Tables S4 and S5 in Supporting Information S2) and fluxes decreased with depth. In GP16, pBa_{xs} flux maxima were usually observed at depths of 200–800 m (148–227 μmol m^{-2} $year^{-1}$ and 157–471 μmol m^{-2} $year^{-1}$ in the western and eastern basins, respectively, Tables S4 and S5 in Supporting Information S2). The magnitude of pBa_{xs} flux was similar in the western and eastern basins of GA03; in contrast, along GP16, fluxes in the eastern basin were generally higher than in the western basin. At stations near the continental margins (e.g., GA03 stations KN199: 1–3, KN204: 1–3, and GP16 station TN303: 1), fluxes in the 2,000–3,000 m range were roughly equivalent to or exceeded fluxes in the upper 0–1,000 m.

Discarding those near-shore stations (GA03 stations KN199-1, KN204-1, KN204-2, and KN204-4; GP16 station 1) with significant lateral suspended material inputs (Lam et al., 2015, 2018; Ohnemus & Lam, 2015; Ohnemus et al., 2018), pBa_{xs} dissolution upon settling through the water column was estimated by subtracting the average 2,000–3,000 m pBa_{xs} flux from the average 0–1,000 m pBa_{xs} flux (Table 2, Tables S4 and S5 in Supporting Information S2). In the North Atlantic pBa_{xs} fluxes in the upper 1,000 m are similar: 1.2 ± 0.4 × 10^2 and 1.5 ± 0.5 × 10^2 μmol m^{-2} $year^{-1}$ (mean and standard deviation) in the eastern and western basins of GA03, respectively. Also, average pBa_{xs} fluxes in the 2,000–3,000 m depth interval in GA03 were not significantly different (p < 0.05), 0.5 ± 0.3 × 10^2 and 0.4 ± 0.2 × 10^2 μmol m^{-2} $year^{-1}$, between the eastern and western basins, respectively. In the Pacific, average 0–1,000 m pBa_{xs} fluxes in the GP16 eastern and western basins were not significantly different from each other, 1.9 ± 1.2 × 10^2 and 1.6 ± 0.2 × 10^2 μmol m^{-2} $year^{-1}$, respectively. The mean pBa_{xs} flux in the 2,000–3,000 m depth range was significantly higher (p < 0.05) in the eastern GP16 basin (1.3 ± 0.3 × 10^2 μmol m^{-2} $year^{-1}$) than in the western basin (0.9 ± 0.3 × 10^2 μmol m^{-2} $year^{-1}$). Between 0–1,000 and 2,000–3,000 m, pBa_{xs} water column dissolution rates are higher in GA03 (58% and 69% in the eastern and western basins, respectively) than in GP16 (17% and 46% in the eastern and western basins, respectively). This is consistent with the lower barite saturation state of the water column in the Atlantic Ocean (<70% below 1,000 m) (e.g., Jeandel et al., 1996) compared to the Pacific (Figure S8 in Supporting Information S1) although other factors could be involved as described below.

We can double-check the magnitude of these pBa_{xs} flux estimates using a simplistic calculation and second approach. Comparing the 0–1,000 and 2,000–3,000 m pBa_{xs} fluxes (Figures 3 and 4; Tables S4, S5 in Supporting Information S2), there is an inferred barite water column dissolution flux of ~100 μmol m^{-2} $year^{-1}$ occurring over the ~2,000 m of intervening water column. If we use an ~1,000 years transit time for deep waters between GA03 and GP16 (e.g., Khatiwala et al., 2012), then these numbers imply an ~50 nmol kg^{-1} interocean difference in deep water dBa due to this water column pBa_{xs} dissolution flux. While the numbers used here are crudely averaged, the results of this simple calculation are nonetheless broadly compatible with our dBa observations. Particle dynamics appear to largely control and explain interocean variability in dBa distributions below ~2,000 m.

Recently, Th-normalized mass AR in modern sediments were compiled into a global database (Costa et al., 2020) and utilized to calculate sedimentary Ba AR (Hayes et al., 2021). AR were available in sediment from cores underlying most of the stations in GP16. The cores were not explicitly dated and the core tops likely represent Holocene material but could contain older sediments. If the sediments are older than modern, the measured excess ^{230}Th will be lower than initial activity due to decay and the pBa_{xs} AR would be overestimated. As an example, an uncorrected age of 25 ka would result in a mass accumulation rate that is about 25% too high. Therefore, the calculated pBaxs AR and burial efficiencies presented in the remainder of this section represent a maximum estimate. In GA03, pBa_{xs} AR were estimated by taking an average of data in the western (n = 7) and eastern

Table 2
Average ^{230}Th-Normalized pBa_{xs} Flux Along GA03 and GP16

	Station	0–1,000 m Avg pBa_{xs} (μmol/m^2/y)	2,000–3,000 m Avg pBa_{xs} (μmol/m^2/yr)	Water column pBa_{xs} dissolution (μmol/m^2/yr)[c]	Percent dissolution (%)	pBa_{xs} AR (μmol/m^2/yr)
GA03						
Eastern basin						
	KN199-1	55	63	−8	−14%	51 ± 47[d]
	KN199-3	116	86	30	26%	
	KN199-5	74	45	29	39%	
	KN199-7	52	12	40	78%	
	KN199-9	150	88	63	42%	
	KN199-10	190	73	117	62%	
	KN199-11	100	51	49	49%	
	KN199-12	112	56	56	50%	
	KN204-24	99	54	45	46%	
	KN204-22	151	29	122	81%	
	KN204-20	163	27	136	83%	
	KN204-18	150	20	130	87%	
Western basin						
	KN204-16	154	21	133	86%	49 ± 40[d]
	KN204-14	208	18	189	91%	
	KN204-12	153	29	124	81%	
	KN204-10	147	38	109	74%	
	KN204-8	199	70	129	65%	
	KN204-6	59	40	19	33%	
	KN204-4	180	102	77	43%	
	KN204-3	97	67	30	31%	
	KN204-2	45	99	−54	−120%	
	KN204-1	32	86	−55	−174%	
Eastern basin	Average	123 ± 41[a]	49 ± 26	74 ± 43	58 ± 21%	51 ± 47[d]
Western basin	Average	153 ± 53[a]	36 ± 19	117 ± 55	69 ± 21%	49 ± 40[d]
GP16						
Eastern basin						
	1	124	188	−67	−52%	
	7	143	136	5	5%	268
	9	434	122	312	72%	546
	11	197	129	69	35%	63
	13	182	110	72	40%	117
	15	154	90	64	42%	
	17	82	101	−19	−24%	57
	18	130	47	84	64%	
Western basin						

Table 2
Continued

	Station	0–1,000 m Avg pBa_{xs} ($\mu mol/m^2/y$)	2,000–3,000 m Avg pBa_{xs} ($\mu mol/m^2/yr$)	Water column pBa_{xs} dissolution ($\mu mol/m^2/yr$)[c]	Percent dissolution (%)	pBa_{xs} AR ($\mu mol/m^2/yr$)
	21	159	53	107	67%	
	23	177	81	96	54%	
	25	173	83	90	52%	
	26	137	104	33	24%	36
	28	182	92	90	50%	15
	30	154	114	40	26%	20
	32	210	122	87	42%	39
	36	158	98	60	38%	
Eastern Basin	Avg	188 ± 115[b]	125 ± 33	62 ± 122	17 ± 43%	210 ± 206
Western Basin	Avg	164 ± 24	88 ± 26	76 ± 26	46 ± 15%	28 ± 12

Note. Particle fluxes in the 0–1,000 and 2,000–3,000 m depth intervals (inclusive) were averaged. Dissolution of pBa_{xs} in the water column between these two depth intervals is also presented along with estimated sedimentary ^{230}Th-normalized pBa_{xs} accumulation rates (AR).

[a]Does not include GA03 stations KN199-1, KN204-1, KN204-2, and KN204-4. [b]Does not include GP16 stations 2–5. [c]Dissolution of pBa_{xs} calculated by subtracting average 2,000–3,000 m flux from 0 to 1,000 m flux. [d]North Atlantic average of available AR between 19° and 43°N (Hayes et al., 2021).

($n = 7$) basins between 19° and 43°N (Hayes et al., 2021). Using these mass AR, we were also able to examine the contribution of post-depositional sedimentary barite dissolution to nonconservative dBa distributions.

From the 2,000–3,000 m depth interval to the seafloor, there may be further pBa_{xs} dissolution. We define a Ba regeneration rate or flux similar to what has been defined and used for Ba in prior studies (Dickens et al., 2003; Paytan & Kastner, 1996); where the Ba regeneration rate is equal to the pBa_{xs} production rate in the mesopelagic zone minus the pBa_{xs} mass accumulation rate in underlying sediment. Ba regeneration can be expressed as a flux or a percentage. We also define a pBa_{xs} burial efficiency as the pBa_{xs} accumulation rate divided by the pBa_{xs} production rate in the mesopelagic zone. Average Th-normalized sedimentary pBa_{xs} AR in the North Atlantic are similar to 2,000–3,000 m pBa_{xs} fluxes in GA03 (Table 2), implying that little of the remaining 2,000–3,000 m pBa_{xs} dissolves in transit from 3,000 m to the sediment-water interface at GA03. Along GP16, average pBa_{xs} sedimentary AR in the western and eastern basins were 28 ± 12 and 210 ± 206 μmol m^{-2} $year^{-1}$, respectively (Figure 4, Table 2) (Hayes et al., 2021). In the western basin, pBa_{xs} ARs are <50% of pBa_{xs} fluxes in 2,000–3,000 m of the water column. AR indicate that either (a) a further ~66%–84% of pBa_{xs} dissolution occurs between 3,000 m and the seafloor, or (b) pBa_{xs} is diagenetically remobilized or dissolves in sediment post-deposition (Figure 4, Table 2). In the eastern GP16 basin, pBa_{xs} ARs often equal or surpass water column pBa_{xs} fluxes at 2,000–3,000 m, indicating that mean Ba regeneration rates are ~0% in this region. At stations 7 and 9, pBa_{xs} ARs exceed the water column pBa_{xs} fluxes in the top 1,000 m. This eastern basin is characterized by extensive benthic nepheloid layers and lateral South American continental margin inputs (Lam et al., 2018; Ohnemus et al., 2018), which may impact the accuracy of the Th-normalization method in this portion of GP16 (Costa et al., 2020). We expect uncertainty in the Th-normalization method to be within about 30% in most of the ocean (Costa et al., 2020).

In the western basin of GP16, substantial pBa_{xs} dissolution occurs despite the fact that water column barite saturation indices are at or above 100% (Figure S8 in Supporting Information S1). As discussed above, the possibility that not all pBa_{xs} is in the form of barite is unlikely, given that other phases presumed to contribute to pBa_{xs} (e.g., Fe oxides, $CaCO_3$, POC, or acantharians) are poorly or negatively correlated with excess pBa (Figures S6 and S7 in Supporting Information S1). The results suggest that water column barite saturation alone may not be the predominant control on pBa_{xs} preservation in deep waters or sediment (Dymond et al., 1992; Eagle et al., 2003). Bottom water oxygen concentrations are lower in the western basin of GP16 than the western basin of GA03

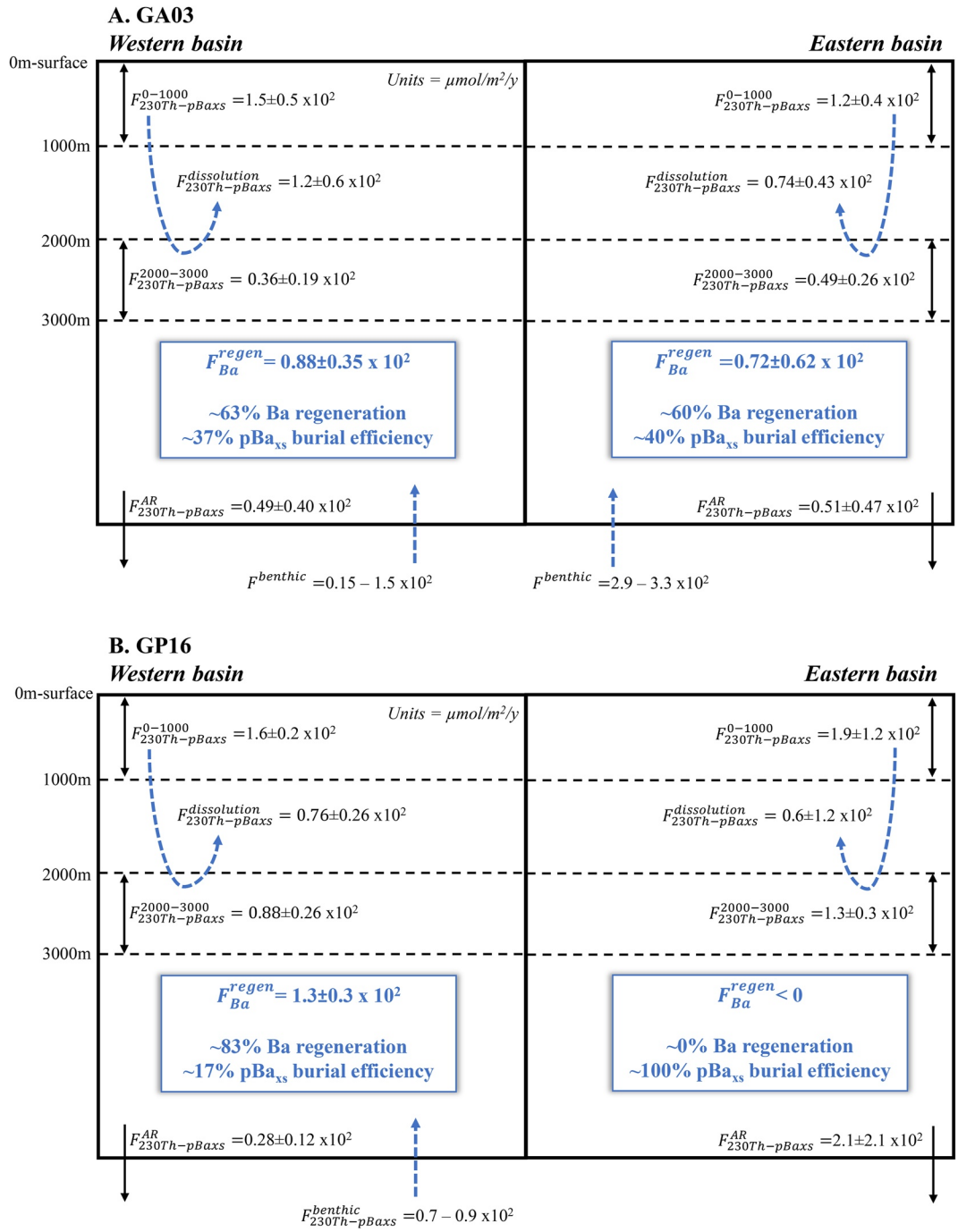

Figure 4. Average mass budgets of the water column pBa_{xs} sinking flux, sedimentary pBa_{xs} AR, Ba regeneration rates, and burial efficiencies in the eastern and western basins of (a) GA03 and (b) GP16. Burial efficiency is defined as the average Th-normalized pBa_{xs} AR ("$F_{230Th-pBaxs}^{MAR}$") divided by the average Th-normalized pBa_{xs} flux within the 0–1,000m layer ("$F_{230Th-pBaxs}^{0-1,000}$") of the water column. The Ba regeneration rate ("F_{Ba}^{regen}") is the difference between the average Th-normalized pBa_{xs} flux within the 0–1,000 m layer and the average Th-normalized pBa_{xs} AR, whereas the water column pBa_{xs} dissolution rate ("$F_{230Th-pBaxs}^{dissolution}$") is the difference between the average flux within the 0–1,000 m layer and the average flux within the 2,000–3,000 m layer ("$F_{230Th-pBaxs}^{2,000-3,000}$"). Benthic fluxes of dissolved Ba in GA03 were estimated from literature values. In the western basin of GP 16, the benthic flux was estimated by subtracting the average flux in the 2,000–3,000 m layer from the average Th-normalized pBa_{xs} AR. The difference between Ba regeneration and burial efficiencies was not significantly different between the eastern and western basins of GA03, whereas regeneration rates and burial efficiencies differed between the eastern and western basins of GP16. High-resolution depth specific fluxes are represented in Figure 3 and Tables S4 and S5 in Supporting Information S2 for each station.

(Figure S1 in Supporting Information S1). Higher mass AR, higher pBa_{xs} concentrations, and oxic conditions all favor pBa_{xs} preservation in sediment (Dymond et al., 1992).

In some circumstances, 1D vertical mass budgets cannot be constrained because lateral transport is significant. For example, near ocean boundaries with high sediment flux or resuspension, the assumptions governing the use of excess dissolved ^{230}Th activities to derive particle flux (e.g., Costa et al., 2020; Pavia et al., 2018) do not always hold due to boundary scavenging (Bacon, 1988; Bruland & Lohan, 2003). Similarly, scavenging of dissolved ^{230}Th (d^{230}Th) and enrichment of p^{230}Th can occur near mid-ocean ridges in hydrothermal plumes with high particle concentrations (Anderson et al., 1983; Hayes et al., 2015; Pavia et al., 2018). For example, high p^{230}Th around hydrothermal plumes will bias water column particle flux derivations by lowering estimates of pBa flux in the water column. In addition, depending on the extent of lateral transport of dissolved ^{230}Th, ^{230}Th-normalized sedimentary fluxes could be biased either high (net transport of dissolved ^{230}Th away from the site) or low (net transport of ^{230}Th toward the site). In GA03, the impact of hydrothermal plumes is limited to <10 km from the MAR (Middleton et al., 2020) and unlikely to have a significant effect on the ^{230}Th-normalized pBa_{xs} fluxes calculated here. At GP16, there is little evidence of such large net lateral transport of dissolved ^{230}Th, which would be apparent as anomalies in the Th-normalized pBa_{xs} flux profiles (Figure 3).

Stable isotope tracer studies provide further evidence of in situ barite formation throughout the mesopelagic zone and dBa regeneration deeper down (e.g., Bates et al., 2017; Geyman et al., 2019; van Beek et al., 2007). For example, profiles of seawater stable Ba isotope compositions ($\delta^{138/134}$Ba) at stations in the Pacific (SAFe, ALOHA) and in the North Atlantic close to KN204 stations (Hydrostation S and JC094 CTD6) are consistent with preferential uptake of isotopically light Ba during the formation of barite (Von Allmen et al., 2010). Uptake leaves ambient waters heavier with subsurface $\delta^{138/134}$Ba maxima of 0.55‰–0.65‰ at 100–300 m, higher than published river end-member values (0.13‰–0.32‰) (Cao et al., 2016, 2020) as well as published water mass end-member values (~0.2‰–0.45‰) (Bates et al., 2017; Geyman et al., 2019; Horner et al., 2015; Hsieh & Henderson, 2017). Below 1,000 m, the profiles at all stations become lighter with depth via slow dissolution of sinking isotopically light barite particles (Bates et al., 2017; Geyman et al., 2019; Hsieh & Henderson, 2017). One estimate of the $\delta^{138/134}$Ba of pBa_{xs} is ~0.09‰ ± 0.01‰ (Bridgestock et al., 2018) with an isotopic fractionation of −0.4‰ to −0.5‰ from the dissolved phase in the waters in which pBa_{xs} forms (Bridgestock et al., 2018; Horner et al., 2017). Depth profiles of stable Ba isotopic compositions at stations in the North Atlantic and North Pacific Oceans thus support the mechanism of in situ barite formation in the mesopelagic zone and dissolution upon settling as a control on nonconservative dBa in the global ocean, discussed in the next section.

Past applications have found that ^{230}Th-normalized fluxes of particulate ^{232}Th, a geochemical tracer of dust, are lower in the upper few hundred meters than for the majority of the water column (Anderson et al., 2016; Pavia et al., 2020; Pérez-Tribouillier et al., 2020). Although hypotheses have been proposed to explain this behavior (Pavia et al., 2020; Pérez-Tribouillier et al., 2020), none have been tested and it is unknown if the bias applies to other particulate phases, such as pBa_{xs}, considered here. Future work may show that the export of particulate pBa_{xs} from the upper 1,000 m of the water column has been underestimated in this study, in which case the estimated rate of particulate pBa_{xs} dissolution will be revised upward and Ba will be less conservative than inferred here.

3.4. Nonconservative dBa

Results of $[Ba]_{nc}$ derived using average water mass end-member dBa concentrations show that though dBa does not behave completely conservatively in either basin, most of the dBa distributions are consistent with conservative water mass mixing (Figures 5a and 5b, Figures S9, S10 and S11 in Supporting Information S1). There were several potential end-member Ba values for most water masses along all the transects (Table S1 and S2 in Supporting Information S1). Another source of "error" in this type of exercise is that OMP Analysis assumes one composition for each end-member taken from one depth at one station, whereas there is likely a distribution of properties and sources characterizing a given water mass (Holzer & Primeau, 2008). Note that the Jenkins, Lott, et al. (2015) and Jenkins, Smethie, et al. (2015) deconvolution results in the placement of DSOW above ISOW even though there is general agreement in the literature that DSOW is the denser of the two water masses (Behrens et al., 2017; LeBel et al., 2008). This seemingly contradictory result (which Jenkins et al. acknowledge) is likely a result of the simplifications inherent in the OMPA deconvolution approach. However, it should not

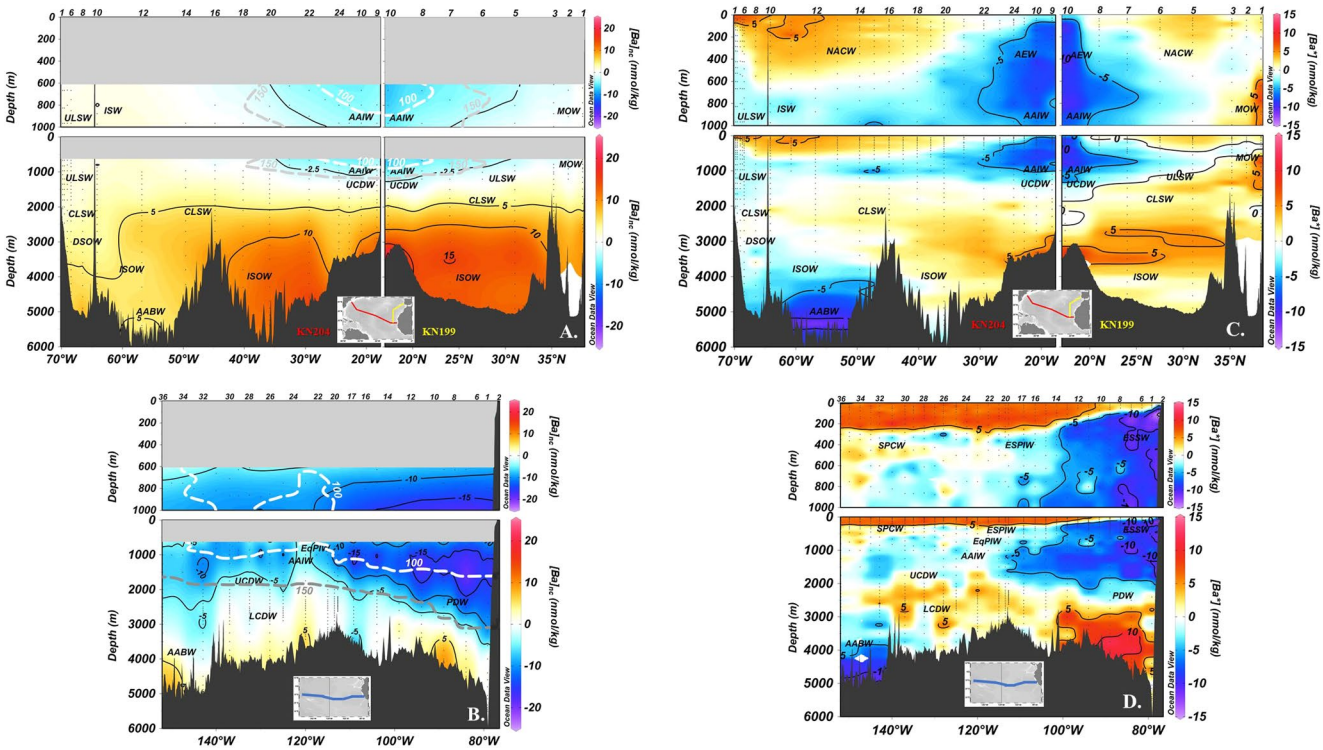

Figure 5. Nonconservative Ba ($[Ba]_{nc}$) distributions in the North Atlantic (a) and East Pacific (b) derived using average end-member water mass dBa concentrations. White- and gray-dashed lines show the 100 and 150 μmol kg^{-1} O_2 contours, respectively. Nonconservative Ba exhibits some correlation with tracer distributions of Ba* along (c) GA03 and (d) GP16 (Supporting Information), where different formulations for Ba* are used for each section as defined in Section 3.5 of the main text. In these and the following figures, see Jenkins, Lott, et al. (2015) and Jenkins, Smethie, et al. (2015) (AEW-Atlantic Equatorial Water; NACW-North Atlantic Central Water; SACW-South Atlantic Central Water; AABW-Antarctic Bottom Water; DSOW-Denmark Strait Overflow Water; ISOW-Iceland-Scotland Overflow Water; CLSW-Classical Labrador Sea Water; MOW-Mediterranean Overflow Water; ULSW-Upper Labrador Sea Water; UCDW-Upper Circumpolar Deep Water; AAIW-Antarctic Intermediate Water; ISW_Irminger Sea Water) and Peters et al. (2018) (ESSW-Equatorial Subsurface Water; ESPIW-Easter South Pacific Intermediate Water; SPCW-South Pacific Central Water; AAIW-Antarctic Intermediate Water; EqPIW-Equatorial Pacific Intermediate Water; UCDW-Upper Circumpolar Deep Water; PDW-Pacific Deep Water LCDW-Lower Circumpolar Deep Water; AABW-Antarctic Bottom Water) for the definitions of the abbreviated water mass labels.

affect our application of the OMPA since we chose end-member dBa concentrations based on the location of the OMPA end-members, not on the composition of "textbook" end-members. The inherent simplification of the OMPA approach is also why herein we pursue several means of interpreting the dBa distribution.

Different combinations of water mass end-member values can be used to (a) highlight the uncertainties in estimating $[Ba]_c$ and (b) determine whether regions of $[Ba]_{nc}$ remained consistent irrespective of end-member selection. Because the extent of nonconservative behavior identified in applications of water mass deconvolution is inherently tied to the distance of the OMPA end-members from the section, the reader is cautioned not to focus too much on magnitudes or percentages of nonconservative behavior. Rather, it is the consistent observation of nonconservative (either source or sink) behavior that is important.

In the Atlantic Ocean, we observed significant average positive excursions from predicted $[Ba]_c$ of 5–20 nmol kg^{-1} below 1,500 m, whereas negative nonconservative Ba concentrations were seen in the OMZ. Our results for $[Ba]_{nc}$ in the northeast end of the GA03 section near Lisbon (Figure 5a) are similar to those of Le Roy et al. (2018) from an overlapping region of section GA01. In the Pacific Ocean, negative $[Ba]_{nc}$ of 5–25 nmol kg^{-1} was present from the continental margin to Tahiti (upper 2,000 m in the west; deepening to >3,000 m in the east; Figure 5b). Positive $[Ba]_{nc}$ ~5 to 10 nmol kg^{-1} was only present in bottom waters near the seafloor. Irrespective of water mass end-member dBa values, for both transects $[Ba]_{nc}$, was negative in the upwelling zone OMZs and tended to be positive in the 500–1,000 m above the sediments. Negative $[Ba]_{nc}$ in the OMZ of GP16 tended to be a higher percentage of total dBa than in the GA03 OMZ (Figure S11 in Supporting Information S1). Indeed, most of GP16 is characterized by $[Ba]_{nc}$ <0, whereas most of GA03 is characterized by $[Ba]_{nc}$ >0 (Figure 5).

The distributions of high pBa_{xs} in both basins are broadly aligned with negative $[Ba]_{nc}$ in the upper water column, except in the regions near the margins with high particle resuspension or nepheloid layers (Figures 2 and 5). This is consistent with in situ water column formation of solid phase barite linked to organic matter respiration and adsorption onto solid phases. Dissolution of barite at depth upon settling through the water column, desorption from or dissolution of solid phases with their minor Ba contents, benthic inputs, continental margin inputs via SGD, and possible hydrothermal inputs will lead to positive $[Ba]_{nc}$. A different choice of location for the origin of PDW in the Peters et al. (2018) OMPA, a location further north than 21°N latitude with a lower dBa end-member value (e.g., Bostock et al., 2010), would likely have led to more positive $[Ba]_{nc}$ considering that >80% of pBa_{xs} that forms in the subsurface in the western basin dissolves. Using Ba:Si and Ba:^{226}Ra correlations as well as particulate phase Ba distributions and prior Ba studies, we examine these processes in detail in the following sections and offer explanations of nonconservative Ba behavior in these transects.

3.5. Relationships Between Ba, Si, and ^{226}Ra and Interpreting Deviations in Their Behavior

In the ocean, dBa, Si, and ^{226}Ra are highly correlated (Bates et al., 2017; Chan et al., 1976; Chung, 1980; Ku & Lin, 1976; Le Roy et al., 2018). Like the water mass tracers N* (Anderson & Sarmiento, 1994) and P* (Broecker et al., 1991), the Ba-Si, Ba-^{226}Ra, and Si-^{226}Ra relationships likely reflect a combination of factors affecting all of these tracers, including high preformed values for many water masses set in the Southern Ocean (e.g., Vance et al., 2017), deep water benthic sources (Chan et al., 1976; Paytan & Kastner, 1996), shallow water continental margin sources (e.g., Ho, Shim, et al., 2019), and particle remineralization (e.g., Dehairs et al., 1980). Deviations from these operationally defined relationships can reveal several important features. Below, we formally define two tracers: Ba* and Ba^{**}_{226Ra} and quantify them here using section-specific relationships (Figure 5, Figures S12 and S13 in Supporting Information S1). The empirical correlations between Ba, Si, and ^{226}Ra tend to arise because of (a) the importance of conservative mixing for the three distributions, (b) large changes in preformed values among water masses, and (c) substantial correlation between preformed values of these elements. Thus, we expect the star relationships to break down in places where nonconservative processes dissimilarly affect these elements. In other words, this is a simple, empirical method to look for nonconservative behavior, and we note, for instance, that deviations in Ba* could relate to nonconservative behavior of either Ba or Si.

Because we are not following the evolution of the Ba-Si, Ba-^{226}Ra, and Si-^{226}Ra relationships during ocean circulation (e.g., Horner et al., 2015), globally defined relationships were not used (i.e., Bates et al., 2017). For GA03, the two tracers are defined as follows (Figures S12a and S12c in Supporting Information S1):

$$Ba^{*} = [Ba]_{meas.} - 0.87 \times [Si]_{meas.} - 38.2$$

$$Ba^{**}_{Ra} = [Ba]_{meas.} - 3.88 \times [^{226}Ra]_{meas.} - 8.3$$

whereas for GP16 (Figures S12b and S12d in Supporting Information S1), they are defined as

$$Ba^{*} = [Ba]_{meas.} - 0.76 \times [Si]_{meas.} - 26.4$$

$$Ba^{**}_{Ra} = [Ba]_{meas.} - 4.51 \times [^{226}Ra]_{meas.} - 3.31$$

The units of the "starred" tracers above are the same as the units of the measured tracers (i.e., nmol kg^{-1} for dBa, µmol kg^{-1} for dSi, and dpm $100L^{-1}$ for ^{226}Ra). Geometric slopes and intercepts ($r > 0.94$) were determined from Type II regressions of element-element correlation plots (Figure S12 in Supporting Information S1) and relative errors in the slopes and intercepts were <1%. The remainder of the discussion will focus on interpretations of the tracer Ba*. Details of the interpretations of Ba^{**}_{226Ra} are provided in the Supporting Information. Generally, between the two basins, we see deviations up to ~30% from dBa values predicted from Ba/Si and Ba/^{226}Ra (Supporting Information). These elements are well correlated along the transects, consistent with observations and conclusions from prior studies (Bates et al., 2017; Chan et al., 1976; Charette et al., 2015; Horner et al., 2015; Le Roy et al., 2018; Wolgemuth, 1970).

The dissolved Ba-Si ratios in GA03 and GP16, 0.76–0.87 nmol Ba/µmol Si (Figure S12 in Supporting Information S1), are within the range of previously reported ratios: 0.52 nmol Ba/µmol Si in the South Atlantic (Horner et al., 2015) and 0.96 nmol Ba/µmol Si in the sub-polar North Atlantic (Le Roy et al., 2018). An average ratio derived from all the GEOSECS cruises (n = 1,505) was 0.630 ± 0.002 nmol Ba/µmol Si (Bates et al., 2017).

In general, Ba and dSi distributions are not well correlated in the upper ocean (Cao et al., 2016, 2020; Chan et al., 1977; Jacquet et al., 2004, 2007), which we also see in GA03 and GP16, in part because Ba is not actively taken up by diatoms (Sternberg et al., 2005).

In both GA03 and GP16, positive and negative Ba* broadly tracks regions of positive and negative $[Ba]_{nc}$ derived using water mass deconvolutions (Figure 5, Figure S14 in Supporting Inforamtion S1). In both ocean basins, Ba* and $[Ba]_{nc}$ were negative within the OMZs. The results are consistent with the formation of barite, corroborated by subsurface maxima in Th-normalized pBa_{xs} fluxes (Figure 3) in GA03 and GP16 OMZs, which occurs in regions of high O_2 utilization and which consumes dBa (Bishop, 1988; Dehairs et al., 1980, 2008; Shopova et al., 1995). The Ba* features are further amplified by biogenic opal dissolution, which releases dSi (Brzezinski & Jones, 2015; Ehlert et al., 2012; Esther et al., 2010; Franz et al., 2012; Hautala & Hammond, 2020; Holzer & Brzezinski, 2015; Ohnemus et al., 2019). Zones of positive Ba* were observed in the western GA03 transect and are consistent with a shelf source of dBa (Section 3.7). Generally, Ba* is correlated with OMPA derived $[Ba]_{nc}$ ($r^2 = 0.41$–0.71), independently substantiating the dominant control of water mass mixing on the dBa distribution in GA03 and GP16.

Changes in Ba* and $[Ba]_{nc}$ were generally coherent below ~2,000 m in the eastern basins of GA03 and GP16 and between 2,000 and 4,000 m depth range in both western basins. Positive deviations are consistent with pBa_{xs} dissolution upon settling through the water column, substantiated by declines in Th-normalized pBa_{xs} fluxes at similar depth ranges from subsurface maxima. In the deepest western basins of both transects, Ba* and average $[Ba]_{nc}$ deviate from each other in part because waters with the most contribution of AABW had negative Ba* with no associated negative $[Ba]_{nc}$. The AABW has a lower Ba/Si (0.83–0.97 mmol/mol, Tables S1 and S2 in Supporting Information S1) than other water masses (1.1–6.4 mmol/mol) observed in GA03 and GP16. The preformed value of AABW likely overprints Ba* in these regions. The impact of differing preformed values is also seen in other tracers, such as stable Si isotopes in GA03 (Brzezinski & Jones, 2015).

3.6. Dissolved Ba Behavior in Oxygen Minimum Zones

Nonconservative [Ba] concentrations are negative in the OMZs of both ocean basins. These regions of negative $[Ba]_{nc}$ overlap regions of high pBa_{xs} ($pBa_{xs} > 175$ pmol/L), negative Ba*, and negative Ba^{**}_{226Ra} (Figures 2c and 5, Figure S13 in Supporting Inforamtion S1). In the GA03 OMZ, average $[Ba]_{nc}$ can be −5 to −10 nmol kg^{-1} (Figure 6a and Figure S9 in Supporting Information S1), whereas in GP16, negative $[Ba]_{nc}$ (Figure 6b and Figure S10 in Supporting Information S1), amounting to −5 to −25 nmol kg^{-1}, is seen across the entire section. Regions with $O_2 < 100$ μmol kg^{-1} are typically associated with the most negative $[Ba]_{nc}$ and the greatest pBa_{xs} (Figures 2c, 2d, and 5b).

These findings provide further supporting evidence of barite formation in microenvironments of decomposing organic matter as it settles through the water column (Bishop, 1988; Dehairs et al., 1980; Gonzalez-Muñoz et al., 2012; Martinez-Ruiz et al., 2019) as the mechanism that removes dBa preferentially to dSi and $d^{226}Ra$, either exclusively or at different Ba/Si or $Ba/^{226}Ra$ ratios within the OMZ than elsewhere in the section. In situ barite formation is also consistent with Th-normalized pBa_{xs} fluxes and reported stable Ba isotope profiles in the two ocean basins (see Sections 3.2 and 3.3). Barite formation in the mesopelagic zone has been suggested as a mechanism to explain observations of negative $[Ba]_{nc}$ in the Arctic Ocean, Mediterranean Sea, and the North Pacific Ocean (Esser & Volpe, 2002; Jullion et al., 2017; Le Roy et al., 2018). We thus conclude that the enhanced barite formation in OMZs leading to negative deviations from conservative dBa behavior is a general oceanic feature.

3.7. Influence of Continental Shelves

Using $d^{228}Ra$ activities, we quantified the input flux of dBa from the east North American continental margin to the western Atlantic Ocean in the same way continental shelf inputs of dissolved Co, Fe, Mn, and Zn were determined (Charette et al., 2016). Though ^{228}Ra ($t_{1/2} = 5.75$ years) has similar sources to ^{226}Ra ($t_{1/2} = 1{,}600$ years), its distribution is controlled largely by the location of Ra major sources (rivers, groundwater, and sediments) and decayed due to its much shorter half-life (Charette et al., 2015). Highest $d^{228}Ra$ activities (4–8 dpm/100 L) and inventories were found in the top 1,000 m of the westernmost stations in GA03 (KN204 stations 1 and

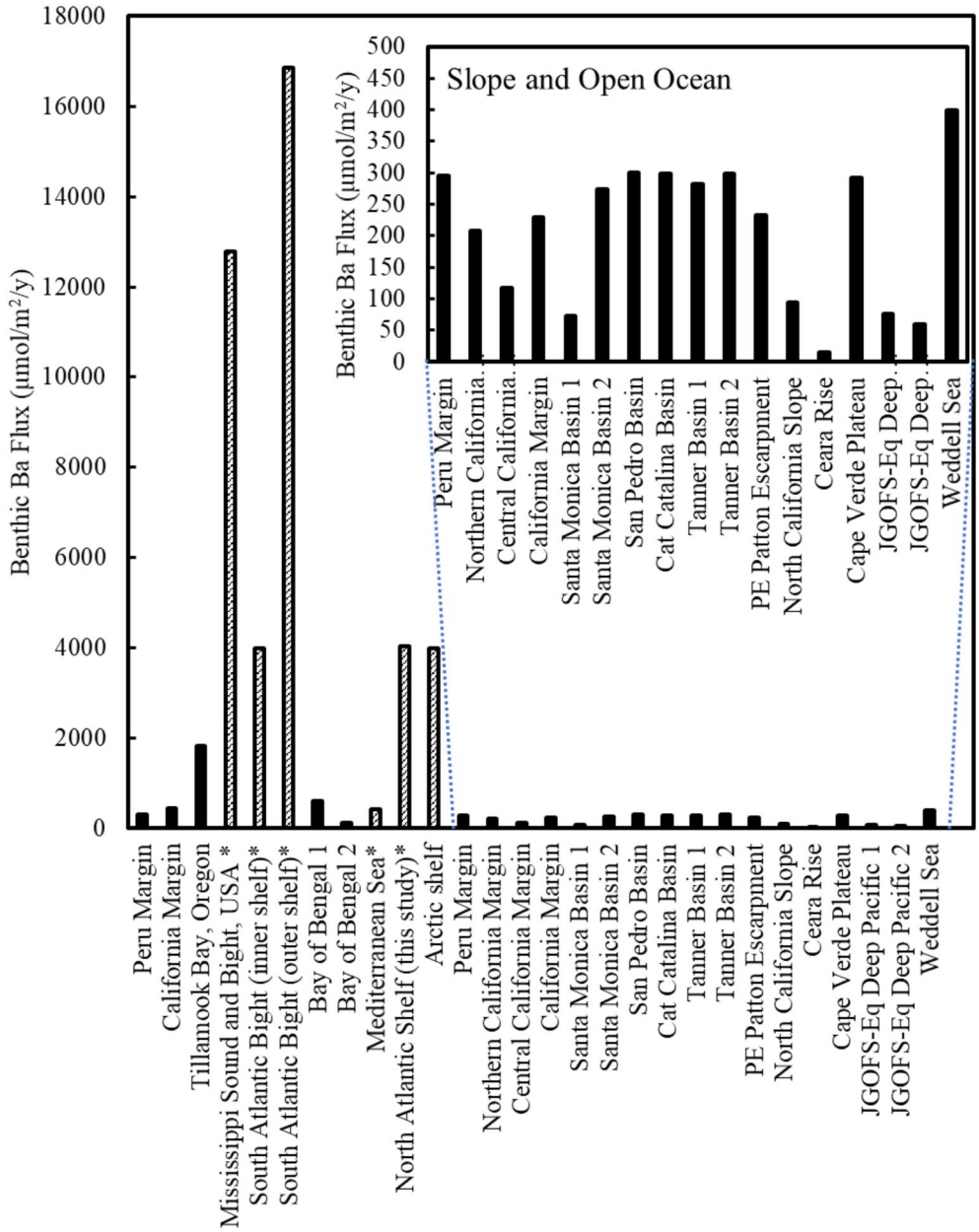

Figure 6. Benthic Ba fluxes from continental margin, slope, and open ocean locations (Table S3 in Supporting Information S1). Minimum estimates are presented for each site and the range can be found in Table S3 in Supporting Information S1. Hashed columns are new flux estimates of net dBa input flux.

2) (Charette et al., 2015; Moore et al., 2008). Roughly, 50% of d^{228}Ra activity in the North Atlantic has been estimated to come from SGD (Moore et al., 2008). In general, ^{228}Ra activity is indicative of waters that have come in recent contact with sediment porewater exchange processes on time scales similar to the half-life of ^{228}Ra. The input flux of dBa can be calculated using the net cross-shelf ^{228}Ra flux modified from Charette et al. (2016):

$$\text{dBa flux} = (^{228}\text{Ra flux}) \times \left(\frac{\Delta \text{dBa}}{\Delta^{228}\text{Ra}}\right) = (^{228}\text{Ra flux}) \times \left(\frac{\text{dBa}_{\text{shelf}} - \text{dBa}_{\text{ocean}}}{^{228}\text{Ra}_{\text{shelf}} - ^{228}\text{Ra}_{\text{ocean}}}\right) \quad (5)$$

where $\text{dBa}_{\text{ocean}}$ and $^{228}\text{Ra}_{\text{ocean}}$ are the average dBa and ^{228}Ra concentration in the open ocean between 0 and 200 m depth, and $\text{dBa}_{\text{shelf}}$ and $^{228}\text{Ra}_{\text{shelf}}$ are the average dBa and ^{228}Ra concentrations in the shelf water column between 0 and

200 m depth. The ^{228}Ra flux for the North Atlantic shelf is 23.9 ± 4.6 × 10^{22} atoms $year^{-1}$, of which 60% is from the western North Atlantic shelves (14.3 ± 1.9 × 10^{22} atoms $year^{-1}$) over a shelf area of 2.5 × 10^{12} m^2 (0–70°N) (Charette et al., 2016; Kwon et al., 2014). The average dBa_{shelf} was estimated in the upper 200 m of the water column at KN204 stations 1 and 2 (45.6 ± 2.5 nmol kg^{-1} = dBa_{shelf}), whereas the average dBa_{ocean} was estimated in the upper 200 m of the water column at KN204 stations 15–17 (41.3 ± 2.3 nmol kg^{-1}). Corresponding average $^{228}Ra_{shelf}$ (0–200 m, KN204 stations 1–2) and $^{228}Ra_{ocean}$ (0–200 m, KN204 stations 14–18) were 3.48 ± 2.7 dpm/100L and 2.08 ± 0.39 dpm/100 L, respectively, leading to ($\Delta dBa/\Delta^{228}Ra$) = 6.9 ± 14 × 10^{-5} nmol/atom. Using these values in Equation 5, the dBa flux from the North Atlantic western continental shelf is 4 ± 8 × 10^3 μmol m^{-2} $year^{-1}$ or approximately 10 ± 20 Gmol $year^{-1}$. Though ΔdBa and $\Delta^{228}Ra$ (Equation 5) are small, average dBa and ^{228}Ra fluxes (i.e., dBa_{shelf}, dBa_{ocean}, $^{228}Ra_{shelf}$, and $^{228}Ra_{ocean}$) are positive and significantly different between shelf and open ocean stations ($p < 0.05$). The high error in dBa flux results from propagating the error associated with ΔdBa and Δ^{228}Ra.

Positive Ba* values of 2–5 nmol kg^{-1} were observed in the upper water column in the western GA03 transect (Section 3.5). If we assume that the additional dBa shelf flux in the western basin, ~4,000 μmol m^{-2} $year^{-1}$, is accurate, then it would take ~33–83 days to see a 2–5 nmol kg^{-1} increase of dBa in the top 200 m over the western shelf region (i.e., for the shelf water volume of 5 × 10^{14} m^3 distributed over 2.5 × 10^{12} m^2 of the shelf area). A shelf source would contribute to both the positive Ba* (Figure 3b) and Ba^{**}_{Ra} (Figure S13 in Supporting Information S1) seen in the upper water column despite pBa_{xs} formation (Figure 2c) and dBa uptake.

The method used to determine the shelf dBa source, based on lateral concentration gradients, derives a net source and not a gross source. The method is insensitive to any recycling of barite on the continental shelf as recycling will have no effect on lateral concentration gradients. Uptake and loss terms are balanced during recycling, so it is only the net source that contributes to the offshore concentration gradients. Though the margin of error is large, our estimate of ~4,000 μmol m^{-2} $year^{-1}$ net dBa addition from the western North Atlantic shelf falls within other estimates of benthic dBa fluxes to the coastal zone (0–200 m water depth, Figure 6, Table S4 in Supporting Information S2) from various continental shelf regions (Ho, Shim, et al., 2019; Moore, 1997; Moore & Shaw, 1998; Roy-Barman et al., 2019; Samanta & Dalai, 2016; Shaw et al., 1998; Whitmore et al., 2021). Indeed, net dBa input from the South Atlantic Bight is ~4,000–16,800 μmol m^{-2} $year^{-1}$ (Moore & Shaw, 1998; Shaw et al., 1998). Flux estimates from other shelf regions (Table S4 in Supporting Information S2) range from 608 μmol m^{-2} $year^{-1}$ to ~54,700 μmol m^{-2} $year^{-1}$ (Bay of Bengal; Moore, 1997).

Several of the estimates in Figure 6 (and Table S4 in Supporting Information S2) for the coastal ocean are inputs of dBa that have otherwise not been accounted for in the global marine Ba budget (Dowling et al., 2003; Ho, Shim, et al., 2019; Moore, 1997; Moore & Shaw, 1998; Roy-Barman et al., 2019; Samanta & Dalai, 2016; Shaw et al., 1998). These new estimates of dBa shelf inputs have been confirmed using Ba/^{228}Ra ratios, regional Ba mass balances, and multiple trace element and stable isotope tracers (Dowling et al., 2003; Ho, Shim, et al., 2019; Moore, 1997; Moore & Shaw, 1998; Roy-Barman et al., 2019; Samanta & Dalai, 2016; Shaw et al., 1998). A recent reevaluation of the Mediterranean Sea Ba cycle revealed that inputs in addition to rivers, dust deposition, and advected water inflowing at the Gibraltar Strait were required to balance the regional marine Ba budget (Roy-Barman et al., 2019). Concomitant release of ^{228}Ra and Ba indicated that inputs via SGD may reconcile the imbalance in the Mediterranean budget (Roy-Barman et al., 2019). Similarly, local mass balances and concomitant ^{226}Ra, ^{228}Ra, and Ba release point to unmistakable SGD sources of Ba to the ocean along the South Atlantic Bight (Moore & Shaw, 1998; Shaw et al., 1998) and the Bay of Bengal (Moore, 1997). Trace element end-member characterizations, direct groundwater dBa measurements, and ^{3}He/^{3}H groundwater-age recharge models have independently verified that SGD can be a significant source of dBa to the Bay of Bengal, seasonally on par with river inputs (Dowling et al., 2003; Samanta & Dalai, 2016). Trace element and isotopic signatures of water mass end-members have been used in the Mississippi Bight and Arctic Ocean to identify substantial shelf sources, likely via SGD, of dBa to the regional ocean (Ho, Shim, et al., 2019; Whitmore et al., 2021).

If we assume that a conservative value for this additional shelf source of dBa to the ocean (i.e., 0.6 mmol m^{-2} $year^{-1}$, Figure 6, Table S3 in Supporting Information S1) is representative of other continental shelf regions, the total additional dBa from the continental shelf, area of 28.8 × 10^{12} m^2 (Rabouille et al., 2001), to the global ocean is at least 17 Gmol $year^{-1}$. Using the conservative value of 0.6 mmol m^{-2} $year^{-1}$ yields a lower estimate of dBa flux from the western Atlantic Shelf (area = 2.5 × 10^{12} m^2) of ~1.7 Gmol $year^{-1}$. Collecting and assessing high-resolution vertical and lateral samples closer to shore for concomitant dBa and ^{228}Ra release (i.e., Moore & Shaw, 1998; Shaw et al., 1998) are needed to help constrain the dBa flux from SGD.

3.8. Hydrothermal Vent Influence

Dissolved Ba, pBa_{xs}, and $[Ba]_{nc}$ distributions did not show much, if any, influence from hydrothermal vents along the North Atlantic and East Pacific transects (Figures 2 and 5, Figures S9, S10 and S15 in Supporting Information S1). Hydrothermal vent fluids from the MAR and EPR can be enriched in dissolved metals, Si, C, stable, and radiogenic isotopes by up to several orders of magnitude above surrounding ambient ocean concentrations (Diehl & Bach, 2020a, 2020b). In the case of barium, reported dBa in hydrothermal vent formation fluids (~0.1 μmol kg^{-1} up to ~98 μmol kg^{-1}, mean 16.6 μmol kg^{-1}) suggests that we are not likely to see a water column influence on its distributions in the two transects nor a significant contribution to oceanic Ba budgets (Diehl & Bach, 2020a, 2020b). The seawater observations most impacted by hydrothermal inputs in GA03 were between 2,600 and 3,500 m at KN204 station 16 (Hatta et al., 2015; Jenkins, Lott, et al., 2015; Measures et al., 2015). In GP16, the most hydrothermally influenced samples were between 2,200 and 2,900 m at station 18 (Jenkins et al., 2018; Resing et al., 2015). Dissolved Mn profiles at GA03 KN204 station 16 and GP16 Station 18 show clear maxima within the MAR and EPR hydrothermal plumes (Hatta et al., 2015; Resing et al., 2015), respectively, with dMn concentrations ~2 orders of magnitude greater than ambient. However, the dBa profiles do not exhibit corresponding maxima at the same depth ranges (Figure S15 in Supporting Information S1). Hydrothermal inputs of dBa are thus minor and do not significantly impact nonconservative Ba distributions along GA03 and GP16.

3.9. Benthic Ba Flux From Deep-Water Sediments

Benthic inputs are an additional source of dBa to both ocean basins (Figure 6, Table S3 in Supporting Information S1). In the deep eastern basin of GA03, a region of high nonconservative [Ba] extends north to Lisbon (Figure 3). Similar dBa anomalies (i.e., positive $[Ba]_{nc}$ of ~5–10 nmol kg^{-1}) below 2,000 m were observed near Lisbon in 2014 during the European GEOVIDE cruise (GEOTRACES GA01) (Le Roy et al., 2018) (Figure S3b in Supporting Information S1). Positive $[Ba]_{nc}$ with increasing depth may in part be due to benthic inputs via dissolution of sedimentary Ba carrier phases (McManus et al., 1998, 1999; Paytan & Kastner, 1996) as well as dissolution of barite as it settles through the water column (Chan et al., 1977). High $d^{228}Ra$ activities and $d^{226}Ra$ (>2 dpm/100L) were found in the same near-bottom samples (Charette et al., 2015), which require a sediment source (Cochran, 1980; Cochran & Krishnaswami, 1980). The ~2 to 4-fold increase in the gradient of dBa with depth in the two deepest samples at KN199-4 stations 10 and 11 (Figure S16 in Supporting Information S1) compared to the gradient in the depths above it indicates that there is a benthic source of Ba to the overlying water column.

There are a few reported values of benthic dBa flux underlying these stations from the Cape Verde Plateau, ranging from 292 to 332 μmol m^{-2} $year^{-1}$ (Rubin et al., 2003). In the North Atlantic, reported benthic Ba fluxes in the western basin at sites from the Ceará Rise range from 15 to 153 μmol m^{-2} $year^{-1}$ (Figure 6, Table S3 in Supporting Information S1, Rubin et al., 2003). Benthic Ba flux measurements were available for locations near GP16 stations: the Peru Margin (296–300 μmol m^{-2} $year^{-1}$) (Rubin et al., 2003) and the Equatorial Deep Pacific (6–1,060 μmol m^{-2} $year^{-1}$) (McManus et al., 1998; Paytan & Kastner, 1996). Benthic inputs, along with barite dissolution in the water column, likely account for the positive $[Ba]_{nc}$ below ~2,000 m in GA03 and the minor positive $[Ba]_{nc}$ observed near the sediment-water interface along GP16.

Using Th-normalized particle sinking flux and mass AR, we see nuanced differences in GA03 and GP16 from prior conceptualizations of the global marine Ba mass balance. Specifically, prior summaries predicted that ~80% of barite that forms in the mesopelagic zone remains intact upon settling to sediment (Dickens et al., 2003; Paytan & Kastner, 1996) and that pBa_{xs} dissolution rates in sediments should be higher in regions underlying high productivity zones than in those underlying lower productivity zones (Paytan & Kastner, 1996). However, in this study, we estimate that only ~30%–40% of pBa_{xs} remains intact during settling from 1,000 m depth in the water column to the seafloor throughout GA03 (Figure 4, Table 3). In the western basin of GP16, instead of ~80% of pBa_{xs} being preserved while settling through the water column, we observe ~80% dissolution (Figure 4, Table 3). And in the high productivity eastern GP16 basin, we observe ~100% burial efficiency (defined as the average Th-normalized pBa_{xs} AR divided by the average Th-normalized pBa_{xs} flux in the 0–1000m layer of the water column) for pBa_{xs} instead of high dissolution rates (Figure 4, Table 3). The margin of error in the average pBa_{xs} AR of the eastern basin is high in GP16 (Figure 4). However, all rates were greater than burial rates underlying the subtropical gyre in the western basin. These are maximum estimates of burial efficiency; if sediments

Table 3
Compilation of Riverine dBa Freshwater (Salinity <0.5) End-Member Concentrations, Annual Specific Yields, and Annual River Input Flux to the Ocean

River	[dBa] (nmol kg^{-1})	Area (10^6 km^2)[f]	Q (km^3 $year^{-1}$)[f]	Specific discharge[g] (L/m^{-2} $year^{-1}$)	dBa-specific yield[h] (μmol m^{-2} $year^{-1}$)	Riverine dBa flux[i] (mol $year^{-1}$)	Refs[j]
Zaire	134.6	3.698	1,200	324	43.7	1.6×10^8	1
Mississippi	462[c]	2.98	262	88	40.7	1.3×10^8	2
Red	371[c]	0.240	35.6	148	55.0	1.6×10^7	2
Changjiang	420	1.810	928	513	216	4.0×10^8	3, 4
Amazon	150[d]	6.110	6,590	1,078	151	9.5×10^8	3, 4,12
Yukon	345	0.849	200	236	81	6.9×10^7	5, 6, 7
Sepik	46.7	0.00787	120	1,525	71	5.7×10^6	3, 4
Danube	242.1	0.8170	207	253	61	5.1×10^7	3, 4
Lena	87.6	2.490	525	211	19	4.7×10^7	3, 4
Colorado	1,025	0.107	2.49	23	24	2.6×10^6	3, 4
Ganges	120.5[b]	1.050	493	470	57	5.9×10^7	8
Brahmaputra	120.5[b]	0.580	510	879	106	6.1×10^7	8
Ganges-Brahmaputra	157[b]	1.630	1,000	613	103	5.3×10^8	9
Pearl	204.5	0.437	363	831	174	7.6×10^7	10
Mackenzie	418[e]	1.787	308	172	90	1.6×10^8	10
Yenisey	24	2.590	620	239	30	7.8×10^7	10
Lena	75	2.490	525	211	27	6.8×10^7	10
Ob	37	2.990	404	135	14	4.0×10^7	10
Pechora	=35[e]	0.348	131	376	38	1.3×10^7	10
Uruguay[a]	208	0.240	145	604	126	3.0×10^7	11
Parana[a]	208	2.783	568	204	43	1.2×10^8	11
Ogooué	128	0.206	137	666	86	1.8×10^7	13
Total	169 ± 100[c]	35×10^6	14,300			3.0×10^9	

Note. The freshwater flux from the sampled rivers comprises 37% of the total annual global freshwater flux to the ocean (global total = 39,080 km^3 $year^{-1}$, Dürr et al. (2011)). The combined drainage basin area of the rivers accounts for 31% of total global exorheic area (i.e., land area that faces the ocean, 114.7×10^6 km^2) (Dürr et al., 2011).

[a]Rivers comprising Rio de la Plata. [b]Average of reported values (Salinity <0.5). [c]Discharge weighted average. [d]Average of concentration reported in Refs. 3 and 12. [e]Average of concentrations reported in Ref. 10 at $S < 1$ (i.e., 410 and 425 nmol kg^{-1} for the Mackenzie River; 25 and 45 nmol kg^{-1} for the Pechora River). [f]Drainage basin area and average annual discharge data from Meybeck & Ragu, 1995. [g]Specific Discharge = (annual discharge)/(drainage basin area). [h]Riverine dBa-Specific yield = ([dBa] × (annual discharge)/(drainage basin area)), assuming the density of freshwater is 1 kg L^{-1}. [i]Riverine flux = [dBa] × discharge, assuming the density of freshwater is 1 kg L^{-1}. [j]References: 1—Edmond et al. (1978); 2—Joung and Shiller (2014); 3—Cao et al. (2016); 4—Cao et al. (2020); 5—Shiller (2003); 6—Shiller (2005a); 7—Shiller (2005b); 8—Moore (1997); 9—Carroll et al. (1993); 10—Guay and Falkner (1998); 11—Hsieh and Henderson (2017); 12—Charbonnier et al. (2020); 13—Moquet et al. (2021).

are significantly older than modern, the burial efficiency may be even lower than estimated for GP16 (e.g., an uncorrected age of 25ka will result in mass accumulation rate, i.e., 25% too high). We expect burial efficiencies underlying OMZs to vary depending on the extent and depth of these zones of high productivity.

The burial efficiency underlying the subtropical gyre in GA03 (~37%, average derived using available pBa_{xs} ARs between 19° and 43°N from Hayes et al. (2021) and we assume it applies to all GA03 stations except KN199-1, KN204-1, KN204-2, and KN204-4; Figure 4) is ~2× higher than the burial efficiency underlying the gyre along GP16 (~17%, TN303 stations 18–36) despite a barite saturation index of <1 in the North Atlantic and >1 along GP16 (Figure S8 in Supporting Information S1). High sediment AR coupled with high pBa_{xs} concentrations likely play a role. Future studies must investigate why such a large fraction of the barite formed in the water column dissolves under supersaturated conditions. In any case, these data represent some of the first high-resolution water column pBa_{xs} fluxes and highlight variability in preservation and regeneration efficiencies in similar biogeochemical provinces in different ocean basins.

3.10. Marine Barium Cycle

In prior summaries of the marine Ba cycle, river dBa inputs to the global ocean are ~15–18 Gmol year^{-1} (Dickens et al., 2003; Paytan & Kastner, 1996). These previous estimates were based on either river end-member concentrations from the Zaire River (Edmond et al., 1978; Paytan & Kastner, 1996) or a series of unnamed rivers in North America (Livingstone, 1963; Wolgemuth & Broecker, 1970). We reassessed this input vector by compiling available dBa concentrations at the mouths of several rivers at salinity <0.5 (Cao et al., 2016, 2020; Carroll et al., 1993; Charbonnier et al., 2020; Edmond et al., 1978; Guay & Falkner, 1998; Hsieh & Henderson, 2017; Joung & Shiller, 2014; Moore, 1997; Moquet et al., 2021; Shiller, 2003, 2005a, 2005b) (Table 3). Together these rivers account for ~40% of the global freshwater discharge to the ocean (Dürr et al., 2011), and their drainage basins account for 31% of total global exorheic area (Dürr et al., 2011). Their combined dBa input flux is 3 Gmol year^{-1}. Taking the discharge weighted average dBa concentration, 169 ± 100 nmol kg^{-1}, we estimate the total river freshwater dBa flux to the ocean is 6.6 ± 3.9 Gmol year^{-1}. This flux is ~2–3*x* lower than in previous models (Dickens et al., 2003; Paytan & Kastner, 1996); however, those summaries combined freshwater dBa river inputs with the dBa that may be released from the suspended particulate matter upon estuarine mixing.

The realization of substantial shelf inputs of dBa may also have implications for explaining the greater surface ocean dBa concentrations in the Atlantic versus the Pacific Ocean. Hsieh and Henderson (2017) and others (e.g., Dehairs et al., 1980; Dickens et al., 2003; Paytan & Kastner, 1996; Wolgemuth & Broecker, 1970) have contended that upwelling of deep waters and river inputs are the major vectors by which dBa is supplied to the surface ocean. Of the two, the estimated upwelling flux (F_{up} = 128 Gmol year^{-1}) is much higher than the river flux. To measure the relative degree of Ba removal from the surface ocean (e.g., via the formation of barite) and the rate of upward mixing of Southern Ocean deep waters, Hsieh and Henderson (2017) defined a Ba utilization index (Ba utilization, defined as $Ba_{utilization} = 1 - ([Ba]_{400\ m}/[Ba]_{SO})$, where $[Ba]_{400\ m}$ are average measured Ba values in <400 m and $[Ba]_{SO}$ is average dBa in the Southern Ocean at depths >2,000 m and assumed to be 99 nmol/kg (Hsieh & Henderson, 2017)). Using their formula, we find Ba utilization along GA03 and GP16, ~57% and ~65%, respectively, similar to the values derived by Hsieh and Henderson (2017) for the Atlantic and North Pacific Oceans, ~55% and ~70%, respectively.

Hsieh and Henderson (2017) suggested that the greater utilization value for the Pacific involves slower vertical mixing rates of upwelled water masses or greater removal related to primary productivity. However, their equation is problematic because (a) it is not deep Southern Ocean water that is the primary upwelled Ba supply in these transects, it is intermediate waters, such as Subantarctic Mode Water and AAIW for the South Pacific and NPIW for the North Pacific (Hartin et al., 2011; Talley, 2013; Toggweiler et al., 1991), and (b) their index does not account for the margin source of Ba, which reflects a greater relative contribution of shelf input in the Atlantic than the Pacific Ocean, due largely to the greater shelf/basin area ratio of the narrower Atlantic Ocean, and thus probably accounts for the apparent interbasin difference in the Ba utilization.

Regarding other dBa inputs, recent studies suggest that hydrothermal vent inputs (Hsieh et al., 2020) of dBa may be lower than the 2–3 Gmol year^{-1} estimated in previous marine budgets (Dickens et al., 2003; Paytan & Kastner, 1996). For the flux from the continent to the ocean, desorption or dissolution of carrier phases along a salinity gradient as riverine sediment loads that enter the ocean has been estimated to be an additional significant flux of dBa to the marine budget, anywhere from 3 to 13 Gmol year^{-1} (Bridgestock et al., 2021) though some work suggests that desorption may be less important to the global Ba marine cycle (Joung & Shiller, 2014). The net addition of new dBa from continental margins (~17 Gmol year^{-1}), likely via SGD, may thus equal or surpass the combined inputs of dBa carried by rivers (i.e., 7 ± 4 Gmol year^{-1}) plus the supply of dBa by desorption from river sediments (3–13 Gmol year^{-1}) on a global scale. The additional continental shelf dBa flux would bring global dBa inputs to at least 29 Gmol year^{-1} (Table 1).

Using a compilation of Th-normalized mass AR (Hayes et al., 2020, 2021), a minimum estimate of the global marine Ba output flux in >1,000 m water depth, via the burial of pBa_{xs}, is ~19 ± 10 Gmol year^{-1}. The inventory of dBa in the ocean is ~150 Tmol. Using the revised range of dBa input fluxes (i.e., 29–44 Gmol year^{-1}, Table 1) and assuming that the marine Ba cycle is in mass balance, the residence time of dBa in the ocean is thus ~3,500–5,000 years rather than ~8,500 years.

The marine Ba isotope budget (Horne & Crockford, 2021) indicates that there must be a major unaccounted dBa source other than rivers and hydrothermal vents: the average $\delta^{138/134}Ba$ of pBa_{xs}, assumed to be the principal

form of Ba output from the ocean, is ∼+0.1‰ (Bridgestock et al., 2018). Rivers and hydrothermal fluids have $\delta^{138/134}$Ba of ∼0.2‰ (Cao et al., 2016, 2020) and −0.17‰ to 0.04‰ (Hsieh et al., 2020), respectively. This additional source may be SGD, the fresh component of which has a $\delta^{138/134}$Ba of +0.1‰ (Mayfield et al., 2021). Estuarine processes will also play a role, where dBa released from river sediment loads has a $\delta^{138}/^{134}$Ba signature that is 0.2‰–0.3‰ lower than the dissolved load (Bridgestock et al., 2021). Given the range of input fluxes (Table 1) and associated $\delta^{138/134}$Ba signatures, the remainder of the shelf source would need to have a $\delta^{138/134}$Ba of 0.09‰–0.18‰ to bring the marine Ba isotope budget into mass balance.

4. Summary and Conclusions

Several processes were investigated to clarify the nonconservative dBa behavior across the North Atlantic and East Pacific transects: (a) in situ water column formation of solid phase barite linked to organic matter respiration; (b) dissolution of barite at depth upon settling through the water column; (c) pBa burial fluxes and fluxes of dBa back to the water column from dissolution of previously sedimented particulate Ba; (d) continental margin inputs, which may be via SGD; and (e) hydrothermal inputs. Of these processes, we found that hydrothermal inputs of dBa from the MAR and EPR had a negligible impact on nonconservative dBa distributions in GA03 and GP16.

While mixing of waters with differing pre-formed dBa is a dominant factor determining the oceanic dBa distribution, nonconservative processes are estimated using OMPA to both supply and remove about 30% of the observed dBa in the North Atlantic and East Pacific transects. Deviations of approximately ±30% were also observed in dBa concentrations predicted from correlations between Ba and Si and between Ba and ^{226}Ra. The transfer of Ba between dissolved and particulate phases plays an important role in controlling the nonconservative dBa behavior in the ocean. In situ formation of barite in OMZs leads to negative deviations from Ba concentrations predicted from water mass mixing. Likely, barite formation in other OMZs in the ocean will lead to similar deviations from the conservative behavior, typically when O_2 falls to <175 μmol kg^{-1} during organic carbon respiration. Regions of negative $[Ba]_{nc}$ extended from 0 to ∼1,000 m in GA03, whereas negative $[Ba]_{nc}$ extended down to ∼2,000–3,000 m in GP16. ^{230}Th-normalized pBa_{xs} fluxes reveal that an estimated ∼65%–85% of particulate Ba dissolved in the water column before the particles reached the sea bed, except in the stations east of the EPR underlying an extensive OMZ. The eastern basin of GP16 had average pBa_{xs} mass AR similar to water column fluxes, suggesting little to no dissolution of barite upon sinking through the water column. The flux of pBa_{xs} in the upper 1,000 m of the water column, derived via normalization to excess particulate ^{230}Th activity, may have been underestimated in this study, in which case pBa_{xs} dissolution rates may be higher than estimated here. In GA03, dissolution of barite either in the water column or in the sediments led to positive deviations from dBa concentrations predicted from water mass mixing. Broadly, pBa_{xs} dissolution in the water column below the mesopelagic zone may explain inter-ocean variability in $[Ba]_{nc}$. Benthic inputs of Ba, though not explicitly calculated in this study, can contribute to positive $[Ba]_{nc}$ in bottom waters near sediment in some parts of the ocean and not others, likely dependent on the extent of active barite formation in the overlying water column.

We also estimate that global river dBa delivery (7 ± 4 Gmol year^{-1}) to the ocean is ∼50% lower than previous estimates. Previously unaccounted for dBa inputs from broad shallow continental margins, inferred to originate from SGD, have been neglected in global marine Ba models. Using ratios of Ba/^{228}Ra, we calculate the western continental shelf of the North Atlantic supplies significant net new dBa to the ocean basin. We estimate that the global net new addition of dBa is equal to or exceeds the combined dissolved plus desorbed particulate Ba global flux from rivers. The shelf source has a large uncertainty, and the ocean dBa budget can be improved by additional measurements of shelf dBa inputs, particularly in regions where high SGD flux is anticipated, such as the Gulf of Mexico. Taken together with revised estimates of global sediment pBa_{xs} AR, the residence time of dBa in the ocean is probably on the order of 3.5–5 kyr, ∼40%–60% lower than previously estimated.

Conflict of Interest

The authors declare no conflicts of interest relevant to this study.

Data Availability Statement

All data supporting the conclusions of this manuscript can be found through the Biological and Chemical Oceanography Data Management Office website (https://www.bco-dmo.org). Additional details supporting the manuscript may be found in the Supporting Information file provided.

Acknowledgments
Many thanks to the captain, crew, and scientists on the R/V Knorr and R/V Thompson during these expeditions. The authors give a special thanks to the in situ pumping group for particle sample collection and processing during the GA03 and GP16 cruises, Martin Fleisher for operating the Lamont-Doherty Earth Observatory ICP-MS facility, Pu Zhang, Larry Edwards, and Hai Cheng at the University of Minnesota for their contributions to the GP16 particulate ^{230}Th concentrations data set, and to Maija Heller and Jong-Mi Lee at UCSC for their measurements of pBa in the GP16 pump samples. The International GEOTRACES Programme is possible in part thanks to the support from the U.S. National Science Foundation (Grant OCE-1840868) to the Scientific Committee on Oceanic Research (SCOR). This research was supported by the National Science Foundation under Grant No. NSF OCE-0927951, NSF OCE-1137851, NSF OCE-1261214, and NSF OCE-1925503 to A. M. Shiller; NSF OCE-1829563 to R. F. Anderson; NSF OCE-0927064 and NSF OCE-1233688 to R. F. Anderson and M. Q. Fleisher; NSF OCE-0927754 to R. Lawrence Edwards; NSF OCE-1233903 to R. Lawrence Edwards and H. Cheng; NSF OCE-0926860 to L. F. Robinson; NSF OCE-0963026 and NSF OCE-1518110 to P. J. Lam; and NSF OCE-1232814 to B. S. Twining.

References

Andersen, M. B., Stirling, C. H., Zimmermann, B., & Halliday, A. N. (2010). Precise determination of the open ocean ^{234}U/^{238}U composition. *Geochemisty, Geophysics, Geosystems*, *11*(12), Q12003. https://doi.org/10.1029/2010GC003318

Anderson, L. A., & Sarmiento, J. L. (1994). Redfield ratios of remineralization determined by nutrient data analysis. *Global Biogeochemical Cycles*, *8*(1), 65–80. https://doi.org/10.1029/93GB03318

Anderson, R. F., Bacon, M. P., & Brewer, P. G. (1983). Removal of ^{230}Th and ^{231}Pa from the open ocean. *Earth and Planetary Science Letters*, *62*(1), 7–23. https://doi.org/10.1016/0012-821X(83)90067-5

Anderson, R. F., Cheng, H., Edwards, R. L., Fleisher, M. Q., Hayes, C. T., Huang, K. F., et al. (2016). How well can we quantify dust deposition to the ocean? *Philosophical Transactions of the Royal Society A: Mathematical, Physical & Engineering Sciences*, *374*(2081), 20150285. https://doi.org/10.1098/rsta.2015.0285

Anderson, R. F., Edwards, R. L., Fleisher, M. Q., & Cheng, H. (2017). *Small and large particulate Th and Pa samples from different depth profiles collected on R/V Thomas G. Thompson in the Eastern Tropical Pacific during 2013 (EPZT Th Pa project)*. Biological and Chemical Oceanography Data Management Office (BCO-DMO). Retrieved from http://lod.bco-dmo.org/id/dataset/676231

Bacon, M. P. (1988). Tracers of chemical scavenging in the ocean: Boundary effects and large-scale chemical fractionation. *Philosophical Transactions of the Royal Society of London – Series A: Mathematical and Physical Sciences*, *325*(1583), 147–160. https://doi.org/10.1098/rsta.1988.0048

Bacon, M. P., & Anderson, R. F. (1982). Distribution of thorium isotopes between dissolved and particulate forms in the deep sea. *Journal of Geophysical Research*, *87*(C3), 2045. https://doi.org/10.1029/jc087ic03p02045

Bacon, M. P., & Edmond, J. M. (1972). Barium at GEOSECS III in the southwest Pacific. *Earth and Planetary Science Letters*, *16*(1), 66–74. https://doi.org/10.1016/0012-821x(72)90237-3

Bates, S. L., Hendry, K. R., Pryer, H. V., Kinsley, C. W., Pyle, K. M., Woodward, E. M. S., & Horner, T. J. (2017). Barium isotopes reveal role of ocean circulation on barium cycling in the Atlantic. *Geochimica et Cosmochimica Acta*, *204*, 286–299. https://doi.org/10.1016/j.gca.2017.01.043

Behrens, E., Våge, K., Harden, B., Biastoch, A., & Böning, C. W. (2017). Composition and variability of the Denmark Strait Overflow Water in a high-resolution numerical model hindcast simulation. *Journal of Geophysical Research: Oceans*, *122*(4), 2830–2846. https://doi.org/10.1002/2016JC012158

Bernstein, R. E., Betzer, P. R., Feely, R. A., Byrne, R. H., Lamb, M. F., & Michaels, A. F. (1987). Acantharian fluxes and strontium to chlorinity ratios in the North Pacific Ocean. *Science*, *237*(4821), 1490–1494. https://doi.org/10.1126/science.237.4821.1490

Bernstein, R. E., & Byrne, R. H. (2004). Acantharians and marine barite. *Marine Chemistry*, *86*(1–2), 45–50. https://doi.org/10.1016/j.marchem.2003.12.003

Bernstein, R. E., Byrne, R. H., & Schijf, J. (1998). Acantharians: A missing link in the oceanic biogeochemistry of barium. *Deep-Sea Research Part I: Oceanographic Research Papers*, *45*(2–3), 491–505. https://doi.org/10.1016/S0967-0637(97)00095-2

Bishop, J. K. B. (1988). The barite-opal-organic carbon association in oceanic particulate matter. *Nature*, *332*(6162), 341–343. https://doi.org/10.1038/332341a0

Black, E. E., Buesseler, K. O., Pike, S. M., & Lam, P. J. (2018). ^{234}Th as a tracer of particulate export and remineralization in the southeastern tropical Pacific. *Marine Chemistry*, *201*(November 2016), 35–50. https://doi.org/10.1016/j.marchem.2017.06.009

Bostock, H. C., Opdyke, B. N., & Williams, M. J. M. (2010). Characterising the intermediate depth waters of the Pacific Ocean using δ^{13}C and other geochemical tracers. *Deep-Sea Research Part I: Oceanographic Research Papers*, *57*(7), 847–859. https://doi.org/10.1016/j.dsr.2010.04.005

Bridgestock, L., Hsieh, Y.-T., Porcelli, D., Homoky, W. B., Bryan, A., & Henderson, G. M. (2018). Controls on the barium isotope compositions of marine sediments. *Earth and Planetary Science Letters*, *481*, 101–110. https://doi.org/10.1016/j.epsl.2017.10.019

Bridgestock, L., Nathan, J., Paver, R., Hsieh, Y.-T., Porcelli, D., Tanzil, J., et al. (2021). Estuarine processes modify the isotope composition of dissolved riverine barium fluxes to the ocean. *Chemical Geology*, *579*(September 2020), 120340. https://doi.org/10.1016/j.chemgeo.2021.120340

Broecker, W. S., Blanton, S., Smethie, W. M., & Ostlund, G. (1991). Radiocarbon decay and oxygen utilization in the Deep Atlantic Ocean. *Global Biogeochemical Cycles*, *5*(1), 87–117. https://doi.org/10.1029/90GB02279

Bruland, K. W., & Lohan, M. C. (2003). Controls of trace metals in seawater. In *Treatise on Geochemistry*, 325.

Bruland, K. W., Rue, E. L., Smith, G. J., & DiTullio, G. R. (2005). Iron, macronutrients and diatom blooms in the Peru upwelling regime: Brown and blue waters of Peru. *Marine Chemistry*, *93*(2–4), 81–103. https://doi.org/10.1016/j.marchem.2004.06.011

Brzezinski, M. A., & Jones, J. L. (2015). Coupling of the distribution of silicon isotopes to the meridional overturning circulation of the North Atlantic Ocean. *Deep-Sea Research Part II: Topical Studies in Oceanography*, *116*, 79–88. https://doi.org/10.1016/j.dsr2.2014.11.015

Buesseler, K. O., & Boyd, P. W. (2009). Shedding light on processes that control particle export and flux attenuation in the twilight zone of the open ocean. *Limnology & Oceanography*, *54*(4), 1210–1232. https://doi.org/10.4319/lo.2009.54.4.1210

Buesseler, K. O., Boyd, P. W., Black, E. E., & Siegel, D. A. (2020). Metrics that matter for assessing the ocean biological carbon pump. *Proceedings of the National Academy of Sciences of the United States of America*, *117*(18), 9679–9687. https://doi.org/10.1073/pnas.1918114117

Cao, Z., Siebert, C., Hathorne, E. C., Dai, M., & Frank, M. (2016). Constraining the oceanic barium cycle with stable barium isotopes. *Earth and Planetary Science Letters*, *434*, 1–9. https://doi.org/10.1016/j.epsl.2015.11.017

Cao, Z., Siebert, C., Hathorne, E. C., Dai, M., & Frank, M. (2020). Corrigendum to "Constraining the oceanic barium cycle with stable barium isotopes" [Earth Planet. Sci. Lett. 434 (2016) 1–9](S0012821X15007219)(10.1016/j.epsl.2015.11.017). *Earth and Planetary Science Letters*, *530*, 116003. https://doi.org/10.1016/j.epsl.2019.116003

Cardinal, D., Alleman, L. Y., Dehairs, F., Savoye, N., Trull, T. W., & André, L. (2005). Relevance of silicon isotopes to Si-nutrient utilization and Si-source assessment in Antarctic waters. *Global Biogeochemical Cycles*, *19*(2). https://doi.org/10.1029/2004GB002364

Carroll, J., Falkner, K. K., Brown, E. T., & Moore, W. S. (1993). The role of the Ganges-Brahmaputra mixing zone in supplying barium and ^{226}Ra to the Bay of Bengal. *Geochimica et Cosmochimica Acta*, *57*(13), 2981–2990. https://doi.org/10.1016/0016-7037(93)90287-7

Chan, L. H., Drummond, D., Edmond, J. M., & Grant, B. (1977). On the barium data from the Atlantic GEOSECS expedition. *Deep-Sea Research*, *24*(7), 613–649. https://doi.org/10.1016/0146-6291(77)90505-7

Chan, L. H., Edmond, J. M., Stallard, R. F., Broecker, W. S., Chung, Y. C., Weiss, R. F., & Ku, T. L. (1976). Radium and barium at GEOSECS stations in the Atlantic and Pacific. *Earth and Planetary Science Letters*, *32*(2), 258–267. https://doi.org/10.1016/0012-821X(76)90066-2

Charbonnier, Q., Bouchez, J., Gaillardet, J., & Gayer, É. (2020). Barium stable isotopes as a fingerprint of biological cycling in the Amazon River basin. *Biogeosciences*, *17*(23), 5989–6015. https://doi.org/10.5194/bg-17-5989-2020

Charette, M. A., Lam, P. J., Lohan, M. C., Kwon, E. Y., Hatje, V., Jeandel, C., et al. (2016). Coastal ocean and shelf-sea biogeochemical cycling of trace elements and isotopes: Lessons learned from GEOTRACES. *Philosophical Transactions of the Royal Society A: Mathematical, Physical & Engineering Sciences*, *374*(2081), 20160076. https://doi.org/10.1098/rsta.2016.0076

Charette, M. A., & Moore, W. S. (2016). *Radium isotopes collected on R/V Thomas G. Thompson cruise TN303 in the Eastern Tropical Pacific in 2013 (U.S. GEOTRACES EPZT project)*. Retrieved from http://lod.bco-dmo.org/id/dataset/650340

Charette, M. A., & Morris, P. J. (2015). *Radium and thorium isotopes sampled by in situ pump on R/V Knorr cruises KN199-04 and KN204-01 in the Subtropical northern Atlantic Ocean from 2010-2011 (U.S. GEOTRACES NAT project)*. Retrieved from http://lod.bco-dmo.org/id/dataset/3846

Charette, M. A., Morris, P. J., Henderson, P. B., & Moore, W. S. (2015). Radium isotope distributions during the US GEOTRACES North Atlantic cruises. *Marine Chemistry*, *177*, 184–195. https://doi.org/10.1016/j.marchem.2015.01.001

Chung, Y. (1980). Radium-barium-silica correlations and a two-dimensional radium model for the world ocean. *Earth and Planetary Science Letters*, *49*(2), 309–318. https://doi.org/10.1016/0012-821X(80)90074-6

Church, T. M., & Wolgemuth, K. (1972). Marine barite saturation. *Earth and Planetary Science Letters*, *15*(1), 35–44. https://doi.org/10.1016/0012-821X(72)90026-X

Cochran, J. K. (1980). The flux of ^{226}Ra from deep-sea sediments. *Earth and Planetary Science Letters*, *49*(2), 381–392. https://doi.org/10.1016/0012-821X(80)90080-1

Cochran, J. K., & Krishnaswami, S. (1980). Radium, thorium, uranium, and Pb^{210} in deep-sea sediments and sediment pore waters from the North Equatorial Pacific. *American Journal of Science*, *280*(9), 849–889. https://doi.org/10.2475/ajs.280.9.849

Collier, R., & Edmond, J. (1984). The trace element geochemistry of marine biogenic particulate matter. *Progress in Oceanography*, *13*(2), 113–199. https://doi.org/10.1016/0079-6611(84)90008-9

Condie, K. C. (1993). Chemical composition and evolution of the upper continental crust: Contrasting results from surface samples and shales. *Chemical Geology*, *104*(1–4), 1–37. https://doi.org/10.1016/0009-2541(93)90140-E

Costa, K. M., Hayes, C. T., Anderson, R. F., Pavia, F. J., Bausch, A., Deng, F., et al. (2020). ^{230}Th normalization: New insights on an essential tool for quantifying sedimentary fluxes in the modern and Quaternary ocean. *Paleoceanography and Paleoclimatology*, *35*(2), 1–36. https://doi.org/10.1029/2019PA003820

Cutter, G. A., & Bruland, K. W. (2012). Rapid and noncontaminating sampling system for trace elements in global ocean surveys. *Limnology and Oceanography: Methods*, *10*(June), 425–436. https://doi.org/10.4319/lom.2012.10.425

Dehairs, F., Chesselet, R., & Jedwab, J. (1980). Discrete suspended particles of barite and the barium cycle in the open ocean. *Earth and Planetary Science Letters*, *49*(2), 528–550. https://doi.org/10.1016/0012-821X(80)90094-1

Dehairs, F., Goeyens, L., Stroobants, N., Bernard, P., Goyet, C., Poisson, A., & Chesselet, R. (1990). On suspended barite and the oxygen minimum in the Southern Ocean. *Global Biogeochemical Cycles*, *4*(1), 85–102. https://doi.org/10.1029/GB004i001p00085

Dehairs, F., Jacquet, S., Savoye, N., Van Mooy, B. A. S., Buesseler, K. O., Bishop, J. K. B., et al. (2008). Barium in twilight zone suspended matter as a potential proxy for particulate organic carbon remineralization: Results for the North Pacific. *Deep-Sea Research Part II: Topical Studies in Oceanography*, *55*(14–15), 1673–1683. https://doi.org/10.1016/j.dsr2.2008.04.020

Dehairs, F., Shopova, D., Ober, S., Veth, C., & Goeyens, L. (1997). Particulate barium stocks and oxygen consumption in the Southern Ocean mesopelagic water column during spring and early summer: Relationship with export production. *Deep-Sea Research Part II: Topical Studies in Oceanography*, *44*(1–2), 497–516. https://doi.org/10.1016/S0967-0645(96)00072-0

Dickens, G. R., Fewless, T., Thomas, E., & Bralower, T. J. (2003). Excess barite accumulation during the Paleocene-Eocene Thermal Maximum: Massive input of dissolved barium from seafloor gas hydrate reservoirs. *Special Papers – Geological Society of America*, *369*(September 2014), 11–23. https://doi.org/10.1130/0-8137-2369-8.11

Diehl, A., & Bach, W. (2020a). *MARHYS database 1.0*. Pangaea. https://doi.org/10.1594/PANGAEA.921794

Diehl, A., & Bach, W. (2020b). MARHYS (MARine HYdrothermal solutions) Database: A global compilation of marine hydrothermal vent fluid, end member, and seawater compositions. *Geochemistry, Geophysics, Geosystems*, *21*(12), 1–17. https://doi.org/10.1029/2020GC009385

Dowling, C. B., Poreda, R. J., & Basu, A. R. (2003). The groundwater geochemistry of the Bengal Basin: Weathering, chemsorption, and trace metal flux to the oceans. *Geochimica et Cosmochimica Acta*, *67*(12), 2117–2136. https://doi.org/10.1016/S0016-7037(02)01306-6

Dürr, H. H., Meybeck, M., Hartmann, J., Laruelle, G. G., & Roubeix, V. (2011). Global spatial distribution of natural riverine silica inputs to the coastal zone. *Biogeosciences*, *8*(3), 597–620. https://doi.org/10.5194/bg-8-597-2011

Dymond, J., & Collier, R. (1996). Particulate barium fluxes and their relationships to biological productivity. *Deep-Sea Research Part II: Topical Studies in Oceanography*, *43*(4–6), 1283–1308. https://doi.org/10.1016/0967-0645(96)00011-2

Dymond, J., Suess, E., & Lyle, M. (1992). Barium in deep-sea sediment: A geochemical proxy for paleoproductivity. *Paleoceanography*, *7*(2), 163–181. https://doi.org/10.1029/92pa00181

Eagle, M., Paytan, A., Arrigo, K. R., van Dijken, G., & Murray, R. W. (2003). A comparison between excess barium and barite as indicators of carbon export. *Paleoceanography*, *18*(1), 1–13. https://doi.org/10.1029/2002pa000793

Edmond, J. M., Boyle, E. D., Drummond, D., Grant, B., & Mislick, T. (1978). Desorption of barium in the plume of the Zaire (Congo) river. *Netherlands Journal of Sea Research*, *12*(3–4), 324–328. https://doi.org/10.1016/0077-7579(78)90034-0

Ehlert, C., Grasse, P., Mollier-Vogel, E., Böschen, T., Franz, J., de Souza, G. F., et al. (2012). Factors controlling the silicon isotope distribution in waters and surface sediments of the Peruvian coastal upwelling. *Geochimica et Cosmochimica Acta*, *99*, 128–145. https://doi.org/10.1016/j.gca.2012.09.038

Esser, B. K., & Volpe, A. M. (2002). At-sea high-resolution chemical mapping: Extreme barium depletion in North Pacific surface water. *Marine Chemistry*, *79*(2), 67–79. https://doi.org/10.1016/S0304-4203(02)00037-3

Esther, T. A., Hammond, D. E., Hautala, S. L., Paul Johnson, H., Schwartz, R. J., & Paukert, A. N. (2010). Evaluation of the budget for silicic acid in Cascadia Basin deep water. *Deep-Sea Research Part I: Oceanographic Research Papers*, *57*(5), 677–686. https://doi.org/10.1016/j.dsr.2010.02.002

Fiz, P., Tréguer, P., Pierre, B., García-Ibáñez, M. I., Pascale, L., & Géraldine, S. (2020). *The 2014 Greenland-Portugal GEOVIDE bottle data (GO-SHIP A25 and GEOTRACES GA01)*. https://doi.org/10.17882/54653

Fogelqvist, E., Blindheim, J., Tanhua, T., Østerhus, S., Buch, E., & Rey, F. (2003). Greenland-Scotland overflow studied by hydro-chemical multivariate analysis. *Deep-Sea Research Part I: Oceanographic Research Papers*, *50*(1), 73–102. https://doi.org/10.1016/S0967-0637(02)00131-0

Francois, R., Honjo, S., Manganini, S. J., & Ravizza, G. E. (1995). Biogenic barium fluxes to the deep sea: Implications for paleoproductivity reconstruction. *Global Biogeochemical Cycles*, *9*(2), 289–303. https://doi.org/10.1029/95GB00021

Franz, J., Krahmann, G., Lavik, G., Grasse, P., Dittmar, T., & Riebesell, U. (2012). Dynamics and stoichiometry of nutrients and phytoplankton in waters influenced by the oxygen minimum zone in the eastern tropical Pacific. *Deep-Sea Research Part I: Oceanographic Research Papers*, *62*, 20–31. https://doi.org/10.1016/j.dsr.2011.12.004

Gao, S., Luo, T. C., Zhang, B. R., Zhang, H. F., Han, Y. W., Zhao, Z. D., & Hu, Y. K. (1998). Chemical composition of the continental crust as revealed by studies in east China. *Geochimica et Cosmochimica Acta*, *62*(11), 1959–1975. https://doi.org/10.1016/S0016-7037(98)00121-5

García-Ibáñez, M. I., Pérez, F. F., Lherminier, P., Zunino, P., Mercier, H., & Tréguer, P. (2018). Water mass distributions and transports for the 2014 GEOVIDE cruise in the North Atlantic. *Biogeosciences*, *15*(7), 2075–2090. https://doi.org/10.5194/bg-15-2075-2018

Gardner, W. D., Biscaye, P. E., & Richardson, M. J. (1997). A sediment trap experiment in the Vema Channel to evaluate the effect of horizontal particle fluxes on measured vertical fluxes. *Journal of Marine Research*, *55*(5), 995–1028. https://doi.org/10.1357/0022240973224139

German, C. R. (2017). *Core-top (0-1cm) sediment data collected by monocore from R/V Thomas G. Thompson TN303 (GP16; EPZT) GEOTRACES cruise from November to December 2013 (GEOTRACES EPZT project)*. Retrieved from http://lod.bco-dmo.org/id/dataset/686982

Geyman, B. M., Ptacek, J. L., LaVigne, M., & Horner, T. J. (2019). Barium in deep-sea bamboo corals: Phase associations, barium stable isotopes, & prospects for paleoceanography. *Earth and Planetary Science Letters*, *525*, 115751. https://doi.org/10.1016/j.epsl.2019.115751

Gonneea, M. E., & Paytan, A. (2006). Phase associations of barium in marine sediments. *Marine Chemistry*, *100*(1–2), 124–135. https://doi.org/10.1016/j.marchem.2005.12.003

Gonzalez-Muñoz, M. T., Martinez-Ruiz, F., Morcillo, F., Martin-Ramos, J. D., & Paytan, A. (2012). Precipitation of barite by marine bacteria: A possible mechanism for marine barite formation. *Geology*, *40*(8), 675–678. https://doi.org/10.1130/G33006.1

Guay, C. K., & Falkner, K. K. (1997). Barium as a tracer of Arctic halocline and river waters. *Deep-Sea Research Part II: Topical Studies in Oceanography*, *44*(8), 1543–1559. https://doi.org/10.1016/S0967-0645(97)00066-0

Guay, C. K., & Falkner, K. K. (1998). A survey of dissolved barium in the estuaries of major Arctic river and adjacent seas. *Continental Shelf Research*, *18*(8), 859–882. https://doi.org/10.1016/S0278-4343(98)00023-5

Haine, T. W. N., Curry, B., Gerdes, R., Hansen, E., Karcher, M., Lee, C., et al. (2015). Arctic freshwater export: Status, mechanisms, and prospects. *Global and Planetary Change*, *125*, 13–35. https://doi.org/10.1016/j.gloplacha.2014.11.013

Hall, J. M., & Chan, L. H. (2004). Ba/Ca in benthic foraminifera: Thermocline and middepth circulation in the North Atlantic during the last glaciation. *Paleoceanography*, *19*(4), 1–13. https://doi.org/10.1029/2004PA001028

Hartin, C. A., Fine, R. A., Sloyan, B. M., Talley, L. D., Chereskin, T. K., & Happell, J. (2011). Formation rates of Subantarctic mode water and Antarctic intermediate water within the South Pacific. *Deep-Sea Research Part I: Oceanographic Research Papers*, *58*(5), 524–534. https://doi.org/10.1016/j.dsr.2011.02.010

Hatta, M., Measures, C. I., Wu, J., Roshan, S., Fitzsimmons, J. N., Sedwick, P., & Morton, P. (2015). An overview of dissolved Fe and Mn distributions during the 2010-2011 U.S. GEOTRACES North Atlantic cruises: GEOTRACES GA03. *Deep-Sea Research Part II: Topical Studies in Oceanography*, *116*, 117–129. https://doi.org/10.1016/j.dsr2.2014.07.005

Hautala, S. L., & Hammond, D. E. (2020). Abyssal pathways and the Double silica maximum in the northeast Pacific basin. *Geophysical Research Letters*, *47*(19), 1–9. https://doi.org/10.1029/2020GL089010

Hayes, C. T., Anderson, R. F., Cheng, H., Conway, T. M., Edwards, R. L., Fleisher, M. Q., et al. (2018). Replacement times of a spectrum of elements in the north Atlantic based on thorium supply. *Global Biogeochemical Cycles*, *32*(9), 1294–1311. https://doi.org/10.1029/2017GB005839

Hayes, C. T., Anderson, R. F., Fleisher, M. Q., Vivancos, S. M., Lam, P. J., Ohnemus, D. C., et al. (2015). Intensity of Th and Pa scavenging partitioned by particle chemistry in the North Atlantic Ocean. *Marine Chemistry*, *170*, 49–60. https://doi.org/10.1016/j.marchem.2015.01.006

Hayes, C. T., Black, E. E., Anderson, R. F., Baskaran, M., Buesseler, K. O., Charette, M. A., et al. (2018). Flux of particulate elements in the north Atlantic Ocean constrained by multiple radionuclides. *Global Biogeochemical Cycles*, *32*(12), 1738–1758. https://doi.org/10.1029/2018GB005994

Hayes, C. T., Costa, K. M., Anderson, R. F., Calvo, E., Chase, Z., Demina, L. L., et al. (2021). Global ocean sediment composition and burial flux in the deep sea. *Global Biogeochemical Cycles*, *35*(4). https://doi.org/10.1029/2020gb006769

Hayes, C. T., Costa, K. M., Calvo, E., Chase, Z., Demina, L. L., Dutay, J.-C., et al. (2020). *Global ocean seafloor sediment geochemistry data during the past 12,000 years*. Retrieved from https://www.ncdc.noaa.gov/paleo-search/study/30512

Heller, M. I., Lam, P. J., Moffett, J. W., Till, C. P., Lee, J. M., Toner, B. M., & Marcus, M. A. (2017). Accumulation of Fe oxyhydroxides in the Peruvian oxygen deficient zone implies non-oxygen dependent Fe oxidation. *Geochimica et Cosmochimica Acta*, *211*(May), 174–193. https://doi.org/10.1016/j.gca.2017.05.019

Henderson, P. B., Morris, P. J., Moore, W. S., & Charette, M. A. (2013). Methodological advances for measuring low-level radium isotopes in seawater. *Journal of Radioanalytical and Nuclear Chemistry*, *296*(1), 357–362. https://doi.org/10.1007/s10967-012-2047-9

Hernandez-Sanchez, M. T., Mills, R. A., Planquette, H., Pancost, R. D., Hepburn, L., Salter, I., & FitzGeorge-Balfour, T. (2011). Quantifying export production in the Southern Ocean: Implications for the Baxs proxy. *Paleoceanography*, *26*(4), PA4222. https://doi.org/10.1029/2010PA002111

Hirose, K. (2006). A new method to determine depth-dependent carbon export fluxes using vertical ^{230}Th profiles. *Geophysical Research Letters*, *33*(5), 9–12. https://doi.org/10.1029/2005GL025129

Ho, P., Resing, J. A., & Shiller, A. M. (2019). Processes controlling the distribution of dissolved Al and Ga along the U.S. GEOTRACES East Pacific Zonal Transect (GP16). *Deep Sea Research Part I: Oceanographic Research Papers*, *147*, 128–145. https://doi.org/10.1016/J.DSR.2019.04.009

Ho, P., Shim, M. J., Howden, S. D., & Shiller, A. M. (2019). Temporal and spatial distributions of nutrients and trace elements (Ba, Cs, Cr, Fe, Mn, Mo, U, V and Re) in Mississippi coastal waters: Influence of hypoxia, submarine groundwater discharge, and episodic events. *Continental Shelf Research*, *175*(January), 53–69. https://doi.org/10.1016/j.csr.2019.01.013

Holzer, M., & Brzezinski, M. A. (2015). Controls on the silicon isotope distribution in the ocean: New diagnostics from a data-constrained model. *Global Biogeochemical Cycles*, *29*(3), 267–287. https://doi.org/10.1002/2014gb004967

Holzer, M., & Primeau, F. W. (2008). The path-density distribution of oceanic surface-to-surface transport. *Journal of Geophysical Research*, *113*(1), 1–22. https://doi.org/10.1029/2006JC003976

Horner, T. J., Kinsley, C. W., & Nielsen, S. G. (2015). Barium-isotopic fractionation in seawater mediated by barite cycling and oceanic circulation. *Earth and Planetary Science Letters*, *430*, 511–522. https://doi.org/10.1016/j.epsl.2015.07.027

Horner, T. J., Little, S. H., Conway, T. M., Farmer, J. R., Hertzberg, J. E., Janssen, D. J., et al. (2021). Bioactive trace metals and their isotopes as paleoproductivity proxies: An assessment using GEOTRACES-era data. *Global Biogeochemical Cycles*, *35*(11). https://doi.org/10.1029/2020gb006814

Horner, T. J., & Crockford, P. W. (2021) *Barium isotopes: Drivers, dependencies, and distributions through space and time*. Cambridge University Press.

Horner, T. J., Pryer, H. V., Nielsen, S. G., Crockford, P. W., Gauglitz, J. M., Wing, B. A., & Ricketts, R. D. (2017). Pelagic barite precipitation at micromolar ambient sulfate. *Nature Communications*, *8*(1). https://doi.org/10.1038/s41467-017-01229-5

Hsieh, Y.-T., Bridgestock, L., Scheuermann, P. P., Seyfried, W. E., & Henderson, G. M. (2020). Barium isotopes in mid-ocean ridge hydrothermal vent fluids: A source of isotopically heavy Ba to the ocean. *Geochimica et Cosmochimica Acta*, *292*, 348–363. https://doi.org/10.1016/j.gca.2020.09.037

Hsieh, Y.-T., & Henderson, G. M. (2017). Barium stable isotopes in the global ocean: Tracer of Ba inputs and utilization. *Earth and Planetary Science Letters*, *473*, 269–278. https://doi.org/10.1016/j.epsl.2017.06.024

Jacquet, S. H. M., Dehairs, F., Dumont, I., Becquevort, S., Cavagna, A. J., & Cardinal, D. (2011). Twilight zone organic carbon remineralization in the polar front zone and subantarctic zone south of Tasmania. *Deep-Sea Research Part II: Topical Studies in Oceanography*, *58*(21–22), 2222–2234. https://doi.org/10.1016/j.dsr2.2011.05.029

Jacquet, S. H. M., Dehairs, F., Elskens, M., Savoye, N., & Cardinal, D. (2007). Barium cycling along WOCE SR3 line in the Southern Ocean. *Marine Chemistry*, *106*(1–2), 33–45. https://doi.org/10.1016/j.marchem.2006.06.007

Jacquet, S. H. M., Dehairs, F., & Rintoul, S. (2004). A high resolution transect of dissolved barium in the Southern Ocean. *Geophysical Research Letters*, *31*(14), 7–10. https://doi.org/10.1029/2004GL020016

Jacquet, S. H. M., Dehairs, F., Savoye, N., Obernosterer, I., Christaki, U., Monnin, C., & Cardinal, D. (2008). Mesopelagic organic carbon remineralization in the Kerguelen Plateau region tracked by biogenic particulate Ba. *Deep-Sea Research Part II: Topical Studies in Oceanography*, *55*(5–7), 868–879. https://doi.org/10.1016/j.dsr2.2007.12.038

Jeandel, C., Dupre, B., Lebaron, G., Monnin, C., & Minster, J. F. (1996). Longitudinal distributions of dissolved barium, silica and alkalinity in the western and southern Indian Ocean. *Deep-Sea Research Part I: Oceanographic Research Papers*, *43*(1), 1–31. https://doi.org/10.1016/0967-0637(95)00098-4

Jenkins, W. J., Lott, D. E., German, C. R., Cahill, K. L., Goudreau, J., & Longworth, B. (2018). The deep distributions of helium isotopes, radiocarbon, and noble gases along the U.S. GEOTRACES East Pacific Zonal Transect (GP16). *Marine Chemistry*, *201*(December 2016), 167–182. https://doi.org/10.1016/j.marchem.2017.03.009

Jenkins, W. J., Lott, D. E., Longworth, B. E., Curtice, J. M., & Cahill, K. L. (2015). The distributions of helium isotopes and tritium along the U.S. GEOTRACES North Atlantic sections (GEOTRACES GAO3). *Deep-Sea Research Part II: Topical Studies in Oceanography*, *116*, 21–28. https://doi.org/10.1016/j.dsr2.2014.11.017

Jenkins, W. J., Smethie, W. M., Boyle, E. A., & Cutter, G. A. (2015). Water mass analysis for the U.S. GEOTRACES (GA03) North Atlantic sections. *Deep-Sea Research Part II: Topical Studies in Oceanography*, *116*, 6–20. https://doi.org/10.1016/j.dsr2.2014.11.018

Joung, D. J., & Shiller, A. M. (2014). Dissolved barium behavior in Louisiana Shelf waters affected by the Mississippi/Atchafalaya River mixing zone. *Geochimica et Cosmochimica Acta*, *141*, 303–313. https://doi.org/10.1016/j.gca.2014.06.021

Jullion, L., Jacquet, S. H. M., & Tanhua, T. (2017). Untangling biogeochemical processes from the impact of ocean circulation: First insight on the Mediterranean dissolved barium dynamics. *Global Biogeochemical Cycles*, *31*(8), 1256–1270. https://doi.org/10.1002/2016GB005489

Kadko, D., Aguilar-Islas, A., Buck, C. S., Fitzsimmons, J. N., Landing, W. M., Shiller, A., et al. (2020). Sources, fluxes and residence times of trace elements measured during the U.S. GEOTRACES East Pacific Zonal Transect. *Marine Chemistry*, *222*(September 2019), 103781. https://doi.org/10.1016/j.marchem.2020.103781

Khatiwala, S., Primeau, F., & Holzer, M. (2012). Ventilation of the deep ocean constrained with tracer observations and implications for radiocarbon estimates of ideal mean age. *Earth and Planetary Science Letters*, *325*(326), 116–125. https://doi.org/10.1016/j.epsl.2012.01.038

Kipp, L. E., Sanial, V., Henderson, P. B., van Beek, P., Reyss, J. L., Hammond, D. E., et al. (2018). Radium isotopes as tracers of hydrothermal inputs and neutrally buoyant plume dynamics in the deep ocean. *Marine Chemistry*, *201*(June 2017), 51–65. https://doi.org/10.1016/j.marchem.2017.06.011

Klump, J., Hebbeln, D., & Wefer, G. (2001). High concentrations of biogenic barium in Pacific sediments after termination I – A signal of changes in productivity and deep water chemistry. *Marine Geology*, *177*(1–2), 1–11. https://doi.org/10.1016/S0025-3227(01)00120-7

Ku, T. L., & Lin, M. C. (1976). ^{226}Ra distribution in the Antarctic Ocean. *Earth and Planetary Science Letters*, *32*(2), 236–248. https://doi.org/10.1016/0012-821X(76)90064-9

Kwon, E. Y., Kim, G., Primeau, F., Moore, W. S., Cho, H.-M., DeVries, T., et al. (2014). Global estimate of submarine groundwater discharge based on an observationally constrained radium isotope model. *Geophysical Research Letters*, *41*(23), 8438–8444. https://doi.org/10.1002/2014GL061574

Lam, P. J. (2018). *Size-fractionated major and minor particle composition and concentration from R/V Knorr KN199-04, KN204-01 in the subtropical North Atlantic Ocean from 2010-2011 (U.S. GEOTRACES NAT project)*. https://doi.org/10.1575/1912/bco-dmo.3871.5.1

Lam, P. J., Lee, J. M., Heller, M. I., Mehic, S., Xiang, Y., & Bates, N. R. (2018). Size-fractionated distributions of suspended particle concentration and major phase composition from the U.S. GEOTRACES Eastern Pacific Zonal Transect (GP16). *Marine Chemistry*, *201*(August 2017), 90–107. https://doi.org/10.1016/j.marchem.2017.08.013

Lam, P. J., Ohnemus, D. C., & Auro, M. E. (2015). Size-fractionated major particle composition and concentrations from the US GEOTRACES North Atlantic zonal transect. *Deep-Sea Research Part II: Topical Studies in Oceanography*, *116*, 303–320. https://doi.org/10.1016/j.dsr2.2014.11.020

LaVigne, M., Hill, T. M., Spero, H. J., & Guilderson, T. P. (2011). Bamboo coral Ba/Ca: Calibration of a new deep ocean refractory nutrient proxy. *Earth and Planetary Science Letters*, *312*(3–4), 506–515. https://doi.org/10.1016/j.epsl.2011.10.013

Lea, D. W. (1993). Constraints on the alkalinity and circulation of glacial circumpolar deep water from benthic foraminiferal barium. *Global Biogeochemical Cycles*, *7*(3), 695–710. https://doi.org/10.1029/93GB01536

Lea, D. W., & Boyle, E. (1989). Barium content of benthic foraminifera controlled by bottom-water composition. *Nature*, *338*(6218), 751–753. https://doi.org/10.1038/338751a0

LeBel, D. A., Smethie, W. M., Jr., Rhein, M., Kieke, D., Fine, R. A., Bullister, J. L., et al. (2008). The formation rate of North Atlantic Deep Water and Eighteen Degree Water calculated from CFC-11 inventories observed during WOCE. *Deep Sea Research Part I: Oceanographic Research Papers*, *55*(8), 891–910. https://doi.org/10.1016/j.dsr.2008.03.009

Lemaitre, N., Planquette, H., Planchon, F., Sarthou, G., Jacquet, S., García-Ibáñez, M. I., et al. (2018). Particulate barium tracing of significant mesopelagic carbon remineralisation in the North Atlantic. *Biogeosciences*, *15*(8), 2289–2307. https://doi.org/10.5194/bg-15-2289-2018

Le Roy, E., Sanial, V., Charette, M. A., van Beek, P., Lacan, F., Henderson, P. B., et al. (2018). The ^{226}Ra-Ba relationship in the north Atlantic during GEOTRACES-GA01. *Biogeosciences*, *15*(November), 3027–3048. https://doi.org/10.5194/bg-15-3027-2018

Li, Y. H., Ku, T. L., Mathieu, G., & Wolgemuth, K. (1973). Ba in the Antarctic Ocean and its implications regarding the marine geochemistry of Ba and ^{226}Ra. *Earth and Planetary Science Letters*, *19*(3), 352–358. https://doi.org/10.1016/0012-821x(73)90085-x

Livingstone, D. A. (1963). Chemical composition of rivers and lakes. In M. Fleischer (Ed.), *Data of Geochemistry* (6th ed., Vol. *440*, pp. G1–G66). Geological Survey. https://doi.org/10.3133/pp440g

Lovecchio, E., Gruber, N., Münnich, M., & Lachkar, Z. (2017). On the long-range offshore transport of organic carbon from the Canary Upwelling System to the open North Atlantic. *Biogeosciences*, *14*(13), 3337–3369. https://doi.org/10.5194/bg-14-3337-2017

Mahowald, N. M., Baker, A. R., Bergametti, G., Brooks, N., Duce, R. A., Jickells, T. D., et al. (2005). Atmospheric global dust cycle and iron inputs to the ocean. *Global Biogeochemical Cycles*, *19*(4). https://doi.org/10.1029/2004GB002402

Martinez-Ruiz, F., Paytan, A., Gonzalez-Muñoz, M. T., Jroundi, F., Abad, M. M., Lam, P. J., et al. (2019). Barite formation in the ocean: Origin of amorphous and crystalline precipitates. *Chemical Geology*, *511*(October 2018), 441–451. https://doi.org/10.1016/j.chemgeo.2018.09.011

Mayfield, K. K., Eisenhauer, A., Santiago Ramos, D. P., Higgins, J. A., Horner, T. J., Auro, M., et al. (2021). Groundwater discharge impacts marine isotope budgets of Li, Mg, Ca, Sr, and Ba. *Nature Communications*, *12*(1), 1–9. https://doi.org/10.1038/s41467-020-20248-3

McCulloch, M., Fallon, S., Wyndham, T., Hendy, E., Lough, J., & Barnes, D. (2003). Coral record of increased sediment flux to the inner Great Barrier Reef since European settlement. *Nature*, *421*(6924), 727–730. https://doi.org/10.1038/nature01361

McManus, J., Berelson, W. M., Hammond, D. E., & Klinkhammer, G. P. (1999). Barium cycling in the North Pacific: Implications for the utility of Ba as a paleoproductivity and paleoalkalinity proxy. *Paleoceanography*, *14*(1), 53–61. https://doi.org/10.1029/1998PA900007

McManus, J., Berelson, W. M., Klinkhammer, G. P., Johnson, K. S., Coale, K. H., Anderson, R. F., et al. (1998). Geochemistry of barium in marine sediments: Implications for its use as a paleoproxy. *Geochimica et Cosmochimica Acta*, *62*(21–22), 3453–3473. https://doi.org/10.1016/s0016-7037(98)00248-8

Measures, C. I., Hatta, M., Fitzsimmons, J., & Morton, P. (2015). Dissolved Al in the zonal N Atlantic section of the US GEOTRACES 2010/2011 cruises and the importance of hydrothermal inputs. *Deep-Sea Research Part II: Topical Studies in Oceanography*, *116*, 176–186. https://doi.org/10.1016/j.dsr2.2014.07.006

Measures, C. I., Landing, W. M., Brown, M. T., & Buck, C. S. (2008). A commercially available rosette system for trace metal-clean sampling. *Limnology and Oceanography: Methods*, *6*(9), 384–394. https://doi.org/10.4319/lom.2008.6.384

Meybeck, M., & Ragu, A. (1995). *GEMS/Water contribution to the global register of river inputs (GLORI), Provisional Final Report* (p. 245). UNEP/WHO/UNESCO.

Michaels, A. F., Caron, D. A., Swanberg, N. R., Howse, F. A., & Michaels, C. M. (1995). Planktonic sarcodines (Acantharia, Radiolaria, foraminifera) in surface waters near Bermuda: Abundance, biomass and vertical flux. *Journal of Plankton Research*, *17*(1), 131–163. https://doi.org/10.1093/plankt/17.1.103

Middleton, J. L., Mukhopadhyay, S., Costa, K. M., Pavia, F. J., Winckler, G., McManus, J. F., et al. (2020). The spatial footprint of hydrothermal scavenging on $^{230}Th_{XS}$-derived mass accumulation rates. *Geochimica et Cosmochimica Acta*, *272*, 218–234. https://doi.org/10.1016/j.gca.2020.01.007

Monnin, C. (1999). A thermodynamic model for the solubility of barite and celestite in electrolyte solutions and seawater to 200°C and to 1 kbar. *Chemical Geology*, *153*(1–4), 187–209. https://doi.org/10.1016/S0009-2541(98)00171-5

Monnin, C., & Cividini, D. (2006). The saturation state of the world's ocean with respect to (Ba,Sr)SO_4 solid solutions. *Geochimica et Cosmochimica Acta*, *70*(13), 3290–3298. https://doi.org/10.1016/j.gca.2006.04.002

Monnin, C., Jeandel, C., Cattaldo, T., & Dehairs, F. (1999). The marine barite saturation state of the world's oceans. *Marine Chemistry*, *65*(3–4), 253–261. https://doi.org/10.1016/S0304-4203(99)00016-X

Moore, W. S. (1997). High fluxes of radium and barium from the mouth of the Ganges-Brahmaputra River during low river discharge suggest a large groundwater source. *Earth and Planetary Science Letters*, *150*(1–2), 141–150. https://doi.org/10.1016/s0012-821x(97)00083-6

Moore, W. S., & Sackett, W. M. (1964). Uranium and thorium series inequilibrium in sea water. *Journal of Geophysical Research*, *69*(24), 5401–5405. https://doi.org/10.1029/jz069i024p05401

Moore, W. S., Sarmiento, J. L., & Key, R. M. (2008). Submarine groundwater discharge revealed by ^{228}Ra distribution in the upper Atlantic Ocean. *Nature Geoscience*, *1*(5), 309–311. https://doi.org/10.1038/ngeo183

Moore, W. S., & Shaw, T. J. (1998). Chemical signals from submarine fluid advection onto the continental shelf. *Journal of Geophysical Research*, *103*(C10), 21543–21552. https://doi.org/10.1029/98JC02232

Moquet, J.-S., Bouchez, J., Braun, J.-J., Bogning, S., Mbonda, A. P., Carretier, S., et al. (2021). Contrasted chemical weathering rates in Cratonic basins: The Ogooué and Mbei rivers, Western Central Africa. *Frontiers in Water*, *2*, 589070. https://doi.org/10.3389/frwa.2020.589070

Ohnemus, D. C., Auro, M. E., Sherrell, R. M., Lagerström, M., Morton, P. L., Twining, B. S., et al. (2014). Laboratory intercomparison of marine particulate digestions including piranha: A novel chemical method for dissolution of polyethersulfone filters. *Limnology and Oceanography: Methods*, *12*(Aug), 530–547. https://doi.org/10.4319/lom.2014.12.530

Ohnemus, D. C., & Lam, P. J. (2015). Cycling of lithogenic marine particles in the US GEOTRACES North Atlantic transect. *Deep-Sea Research Part II: Topical Studies in Oceanography*, *116*, 283–302. https://doi.org/10.1016/j.dsr2.2014.11.019

Ohnemus, D. C., Lam, P. J., & Twining, B. S. (2018). Optical observation of particles and responses to particle composition in the GEOTRACES GP16 section. *Marine Chemistry*, *201*(September 2017), 124–136. https://doi.org/10.1016/j.marchem.2017.09.004

Ohnemus, D. C., Rauschenberg, S., Cutter, G. A., Fitzsimmons, J. N., Sherrell, R. M., & Twining, B. S. (2017). Elevated trace metal content of prokaryotic communities associated with marine oxygen deficient zones. *Limnology & Oceanography*, *62*(1), 3–25. https://doi.org/10.1002/lno.10363

Ohnemus, D. C., Torrie, R., & Twining, B. S. (2019). Exposing the Distributions and elemental associations of scavenged particulate phases in the ocean using basin-scale multi-element data sets. *Global Biogeochemical Cycles*, *33*(6), 725–748. https://doi.org/10.1029/2018GB006145

Owens, S. A., Buesseler, K. O., & Sims, K. W. W. (2011). Re-evaluating the 238U-salinity relationship in seawater: Implications for the ^{238}U-^{234}Th disequilibrium method. *Marine Chemistry*, *127*(1–4), 31–39. https://doi.org/10.1016/j.marchem.2011.07.005

Pavia, F. J., Anderson, R. F., Lam, P. J., Cael, B. B., Vivancos, S. M., Fleisher, M. Q., et al. (2019). Shallow particulate organic carbon regeneration in the South Pacific Ocean. *Proceedings of the National Academy of Sciences of the United States of America*, *116*(20), 9753–9758. https://doi.org/10.1073/pnas.1901863116

Pavia, F. J., Anderson, R. F., Vivancos, S., Fleisher, M., Lam, P., Lu, Y., et al. (2018). Intense hydrothermal scavenging of ^{230}Th and ^{231}Pa in the deep Southeast Pacific. *Marine Chemistry*, *201*(April 2017), 212–228. https://doi.org/10.1016/j.marchem.2017.08.003

Pavia, F. J., Anderson, R. F., Winckler, G., & Fleisher, M. Q. (2020). Atmospheric Dust inputs, iron cycling, and biogeochemical connections in the south Pacific ocean from thorium isotopes. *Global Biogeochemical Cycles*, *34*(9), e2020GB006562. https://doi.org/10.1029/2020GB006562

Paytan, A., & Griffith, E. M. (2007). Marine barite: Recorder of variations in ocean export productivity. *Deep-Sea Research Part II: Topical Studies in Oceanography*, *54*(5–7), 687–705. https://doi.org/10.1016/j.dsr2.2007.01.007

Paytan, A., & Kastner, M. (1996). Benthic Ba fluxes in the central equatorial Pacific, implications for the oceanic Ba cycle. *Earth and Planetary Science Letters*, *142*(3–4), 439–450. https://doi.org/10.1016/0012-821x(96)00120-3

Paytan, A., Kastner, M., & Chavez, F. P. (1996). Glacial to interglacial fluctuations in productivity in the equatorial Pacific as indicated by marine barite. *Science*, *274*(5291), 1355–1357. https://doi.org/10.1126/science.274.5291.1355

Pérez-Tribouillier, H., Noble, T. L., Townsend, A. T., Bowie, A. R., & Chase, Z. (2020). Quantifying lithogenic inputs to the Southern Ocean using long-lived thorium isotopes. *Frontiers in Marine Science*, *7*, 207. https://doi.org/10.3389/fmars.2020.00207

Peters, B. D., Jenkins, W. J., Swift, J. H., German, C. R., Moffett, J. W., Cutter, G. A., et al. (2018). Water mass analysis of the 2013 US GEOTRACES eastern Pacific zonal transect (GP16). *Marine Chemistry*, *201*(September 2017), 6–19. https://doi.org/10.1016/j.marchem.2017.09.007

Planchon, F., Cavagna, A.-J., Cardinal, D., André, L., & Dehairs, F. (2012). Late summer particulate organic carbon export and twilight zone remineralisation in the Atlantic sector of the Southern Ocean. *Biogeosciences Discussions*, *9*(3), 3423–3477. https://doi.org/10.5194/bgd-9-3423-2012

Rabouille, C., Mackenzie, F. T., & Ver, L. M. (2001). Influence of the human perturbation on carbon, nitrogen, and oxygen biogeochemical cycles in the global coastal ocean. *Geochimica et Cosmochimica Acta*, *65*(21), 3615–3641. https://doi.org/10.1016/s0016-7037(01)00760-8

Resing, J. A., Sedwick, P. N., German, C. R., Jenkins, W. J., Moffett, J. W., Sohst, B. M., & Tagliabue, A. (2015). Basin-scale transport of hydrothermal dissolved metals across the South Pacific Ocean. *Nature*, *523*(7559), 200–203. https://doi.org/10.1038/nature14577

Roeske, T., Bauch, D., Rutgers, M., & Rabe, B. (2012). Utility of dissolved barium in distinguishing north American from eurasian runoff in the Arctic Ocean. *Marine Chemistry*, *132–133*, 1–14. https://doi.org/10.1016/j.marchem.2012.01.007

Roeske, T., vd Loeff, M. R., Middag, R., & Bakker, K. (2012). Deep water circulation and composition in the Arctic Ocean by dissolved barium, aluminium and silicate. *Marine Chemistry*, *132*(133), 56–67. https://doi.org/10.1016/j.marchem.2012.02.001

Roy-Barman, M., Pons-Branchu, E., Levier, M., Bordier, L., Foliot, L., Gdaniec, S., et al. (2019). Barium during the GEOTRACES GA-04S MedSeA cruise: The Mediterranean Sea Ba budget revisited. *Chemical Geology*, *511*(August 2018), 431–440. https://doi.org/10.1016/j.chemgeo.2018.09.015

Rubin, S. I., King, S. L., Jahnke, R. A., & Froelich, P. N. (2003). Benthic barium and alkalinity fluxes: Is Ba an oceanic paleo-alkalinity proxy for glacial atmospheric CO_2? *Geophysical Research Letters*, *30*(17), 1–4. https://doi.org/10.1029/2003GL017339

Rudnick, R. L., & Gao, S. (2014). *Composition of the continental crust*. *Treatise on Geochemistry* (2nd ed., Vol. 3, pp. 1–51). Elsevier Ltd. https://doi.org/10.1016/B978-0-08-095975-7.00301-6

Rushdi, A. I., McManus, J., & Collier, R. W. (2000). Marine barite and celestite saturation in seawater. *Marine Chemistry*, *69*(1–2), 19–31. https://doi.org/10.1016/S0304-4203(99)00089-4

Samanta, S., & Dalai, T. K. (2016). Dissolved and particulate Barium in the Ganga (Hooghly) River estuary, India: Solute-particle interactions and the enhanced dissolved flux to the oceans. *Geochimica et Cosmochimica Acta*, *195*, 1–28. https://doi.org/10.1016/j.gca.2016.09.005

Sanial, V., Kipp, L. E., Henderson, P. B., van Beek, P., Reyss, J. L., Hammond, D. E., et al. (2018). Radium-228 as a tracer of dissolved trace element inputs from the Peruvian continental margin. *Marine Chemistry*, *201*(May 2017), 20–34. https://doi.org/10.1016/j.marchem.2017.05.008

Schoepfer, S. D., Shen, J., Wei, H., Tyson, R. V., Ingall, E., & Algeo, T. J. (2015). Total organic carbon, organic phosphorus, and biogenic barium fluxes as proxies for paleomarine productivity. *Earth-Science Reviews*, *149*, 23–52. https://doi.org/10.1016/j.earscirev.2014.08.017

Schroeder, J. O., Murray, R. W., Leinen, M., Pflaum, R. C., & Janecek, T. R. (1997). Barium in equatorial Pacific carbonate sediment: Terrigenous, oxide, and biogenic associations. *Paleoceanography*, *12*(1), 125–146. https://doi.org/10.1029/96PA02736

Shaw, D. M., Dostal, J., & Keays, R. R. (1976). Additional estimates of continental surface Precambrian shield composition in Canada. *Geochimica et Cosmochimica Acta*, *40*(1), 73–83. https://doi.org/10.1016/0016-7037(76)90195-2

Shaw, D. M., Reilly, G. A., Muysson, J. R., Pattenden, G. E., & Campbell, F. E. (1967). An estimate of the chemical composition of the Canadian Precambrain Shield. *Canadian Journal of Earth Sciences*, *4*(5), 829–853. https://doi.org/10.1139/e67-058

Shaw, T. J., Moore, W. S., Kloepfer, J., & Sochaski, M. A. (1998). The flux of barium to the coastal waters of the southeastern USA: The importance of submarine groundwater discharge. *Geochimica et Cosmochimica Acta*, *62*(18), 3047–3054. https://doi.org/10.1016/S0016-7037(98)00218-X

Shelley, R. U., Morton, P. L., & Landing, W. M. (2015). Elemental ratios and enrichment factors in aerosols from the US-GEOTRACES North Atlantic transects. *Deep-Sea Research Part II: Topical Studies in Oceanography*, *116*, 262–272. https://doi.org/10.1016/j.dsr2.2014.12.005

Sherrell, R. M., Twining, B., & German, C. R. (2016). Trace elements in suspended particles from GO-Flo bottles. Biological and Chemical Oceanography data Management Office (BCO-DMO). Version date 2016-05-17. Retrieved from http://lod.bco-dmo.org/id/dataset/639847

Shiller, A. M. (2003). Dissolved and colloidal trace elements. In P. F. Schuster (Ed.), *Water and sediment quality in the Yukon river basin, Alaska during water year 2001 (No. USGS-OFR-03-427)* (pp. 33–36).

Shiller, A. M. (2005a). Dissolved and colloidal trace elements. In P. F. Schuster (Ed.), *Water and sediment quality in the Yukon river basin, Alaska during water year 2003 (No. USGS-OFR-2005-1397)* (pp. 42–46).

Shiller, A. M. (2005b). Dissolved and colloidal trace elements. In P. F.Schuster (Ed.), *Water and sediment quality in the Yukon river basin, Alaska, during water year 2002* (Open-File, pp. 50–53). USGS.

Shiller, A. M. (2016a). Dissolved barium (Ba) from R/V Thomas G. Thompson cruise TN303 (GP16) in the eastern tropical Pacific in 2013 (U.S. GEOTRACES EPZT project). Retrieved from https://www.bco-dmo.org/dataset/648753

Shiller, A. M. (2016b). *Dissolved Ga and Ba from GEOTRACES Rosette bottles R/V Knorr cruises KN199-04 and KN204-01 (GA03) in the subtropical northern Atlantic Ocean from 2010-2011 (U.S. GEOTRACES NAT project)*. Retrieved from https://www.bco-dmo.org/dataset/3827

Shim, M.-J., Swarzenski, P. W., & Shiller, A. M. (2012). Dissolved and colloidal trace elements in the Mississippi River delta outflow after Hurricanes Katrina and Rita. *Continental Shelf Research*, *42*, 1–9. https://doi.org/10.1016/j.csr.2012.03.007

Shopova, D., Dehairs, F., & Baeyens, W. (1995). A simple model of biogeochemical element distribution in the oceanic water column. *Journal of Marine Systems*, *6*(4), 331–344. https://doi.org/10.1016/0924-7963(94)00032-7

Sternberg, E., Tang, D., Ho, T. Y., Jeandel, C., & Morel, F. M. M. (2005). Barium uptake and adsorption in diatoms. *Geochimica et Cosmochimica Acta*, *69*(11), 2745–2752. https://doi.org/10.1016/j.gca.2004.11.026

Stroobants, N., Dehairs, F., Goeyens, L., Vanderheijden, N., & Van Grieken, R. (1991). Barite formation in the Southern Ocean water column. *Marine Chemistry*, *35*(1–4), 411–421. https://doi.org/10.1016/S0304-4203(09)90033-0

Sutton, J. N., De Souza, G. F., García-Ibáñez, M. I., & Rocha, C. L. D. L. (2018). The silicon stable isotope distribution along the GEOVIDE section (GEOTRACES GA-01) of the North Atlantic Ocean. *Biogeosciences*, *15*(18), 5663–5676. https://doi.org/10.5194/bg-15-5663-2018

Talley, L. D. (2013). Closure of the global overturning circulation through the Indian, Pacific and Southern Oceans: Schematics and transports. *Journal of Chemical Information and Modeling*, *53*(9), 1689–1699. https://doi.org/10.1017/CBO9781107415324.004

Tanhua, T., Olsson, K. A., & Jeansson, E. (2005). Formation of Denmark Strait overflow water and its hydro-chemical composition. *Journal of Marine Systems*, *57*(3–4), 264–288. https://doi.org/10.1016/j.jmarsys.2005.05.003

Taylor, S. R., & Mclennan, S. M. (1995). The geochemical evolution of the continental crust. *Reviews of Geophysics*, *33*(2), 241–265. https://doi.org/10.1029/95rg00262

Thomas, H., Shadwick, E., Dehairs, F., Lansard, B., Mucci, A., Navez, J., et al. (2011). Barium and carbon fluxes in the Canadian Arctic Archipelago. *Journal of Geophysical Research*, *116*(12), 1–16. https://doi.org/10.1029/2011JC007120

Toggweiler, J. R., Dixon, K., & Broecker, W. S. (1991). The Peru upwelling and the ventilation of the south Pacific thermocline. *Journal of Geophysical Research*, *96*(C11), 20467. https://doi.org/10.1029/91jc02063

Twining, B. S., Rauschenberg, S., Morton, P. L., Ohnemus, D. C., & Lam, P. J. (2015). Comparison of particulate trace element concentrations in the North Atlantic Ocean as determined with discrete bottle sampling and in situ pumping. *Deep Sea Research Part II: Topical Studies in Oceanography*, *116*, 273–282. https://doi.org/10.1016/j.dsr2.2014.11.005

van Beek, P., François, R., Conte, M., Reyss, J. L., Souhaut, M., & Charette, M. (2007). ^{228}Ra/^{226}Ra and ^{226}Ra/Ba ratios to track barite formation and transport in the water column. *Geochimica et Cosmochimica Acta*, *71*(1), 71–86. https://doi.org/10.1016/j.gca.2006.07.041

Vance, D., Little, S. H., de Souza, G. F., Khatiwala, S., Lohan, M. C., & Middag, R. (2017). Silicon and zinc biogeochemical cycles coupled through the Southern Ocean. *Nature Geoscience*, *10*(3), 202–206. https://doi.org/10.1038/ngeo2890

Von Allmen, K., Böttcher, M. E., Samankassou, E., & Nägler, T. F. (2010). Barium isotope fractionation in the global barium cycle: First evidence from barium minerals and precipitation experiments. *Chemical Geology*, *277*(1–2), 70–77. https://doi.org/10.1016/j.chemgeo.2010.07.011

Whitmore, L. M., Shiller, A. M., Horner, T. J., Xiang, Y., Auro, M. E., Bauch, D., et al. (2021). Strong margin influence on the Arctic Ocean barium cycle revealed by Pan-Arctic synthesis. *Journal of Geophysical Research: Oceans*, 2021JC017417.

Wolgemuth, K. (1970). Barium analyses from the first Geosecs test cruise. *Journal of Geophysical Research*, *75*(36), 7686–7687. https://doi.org/10.1029/jc075i036p07686

Wolgemuth, K., & Broecker, W. S. (1970). Barium in sea water. *Earth and Planetary Science Letters*, *8*(5), 372–378. https://doi.org/10.1016/0012-821X(70)90110-X

References From the Supporting Information

Anderson, R. F., Cheng, H., Edwards, R. L., Fleisher, M. Q., Hayes, C. T., Huang, K. F., et al. (2016). How well can we quantify dust deposition to the ocean? *Philosophical Transactions of the Royal Society A: Mathematical, Physical & Engineering Sciences*, *374*(2081), 20150285. https://doi.org/10.1098/rsta.2015.0285

Anderson, R. F., Edwards, R. L., Fleisher, M. Q., & Cheng, H. (2017). *Small and large particulate Th and Pa samples from different depth profiles collected on R/V Thomas G. Thompson in the Eastern Tropical Pacific during 2013 (EPZT Th Pa project)*. Biological and Chemical Oceanography Data Management Office (BCO-DMO). Retrieved from http://lod.bco-dmo.org/id/dataset/676231

Chan, L. H., Edmond, J. M., Stallard, R. F., Broecker, W. S., Chung, Y. C., Weiss, R. F., & Ku, T. L. (1976). Radium and barium at GEOSECS stations in the Atlantic and Pacific. *Earth and Planetary Science Letters*, *32*(2), 258–267. https://doi.org/10.1016/0012-821X(76)90066-2

Charette, M. A., Morris, P. J., Henderson, P. B., & Moore, W. S. (2015). Radium isotope distributions during the US GEOTRACES North Atlantic cruises. *Marine Chemistry*, *177*, 184–195. https://doi.org/10.1016/j.marchem.2015.01.001

Chung, Y. (1980). Radium-barium-silica correlations and a two-dimensional radium model for the world ocean. *Earth and Planetary Science Letters*, *49*(2), 309–318. https://doi.org/10.1016/0012-821X(80)90074-6

Cochran, J. K. (1980). The flux of ^{226}Ra from deep-sea sediments. *Earth and Planetary Science Letters*, *49*(2), 381–392. https://doi.org/10.1016/0012-821X(80)90080-1

de Souza, G. F., Slater, R. D., Hain, M. P., Brzezinski, M. A., & Sarmiento, J. L., (2015). Distal and proximal controls on the silicon stable isotope signature of North Atlantic Deep Water. *Earth and Planetary Science Letters*, *432*, 342–353. https://doi.org/10.1016/j.epsl.2015.10.025

Ehlert, C., Grasse, P., Mollier-Vogel, E., Böschen, T., Franz, J., de Souza, G. F., et al. (2012). Factors controlling the silicon isotope distribution in waters and surface sediments of the Peruvian coastal upwelling. *Geochimica et Cosmochimica Acta*, *99*, 128–145. https://doi.org/10.1016/j.gca.2012.09.038

Esther, T. A., Hammond, D. E., Hautala, S. L., Paul Johnson, H., Schwartz, R. J., & Paukert, A. N. (2010). Evaluation of the budget for silicic acid in Cascadia Basin deep water. *Deep-Sea Research Part I: Oceanographic Research Papers*, *57*(5), 677–686. https://doi.org/10.1016/j.dsr.2010.02.002

Franz, J., Krahmann, G., Lavik, G., Grasse, P., Dittmar, T., & Riebesell, U. (2012). Dynamics and stoichiometry of nutrients and phytoplankton in waters influenced by the oxygen minimum zone in the eastern tropical Pacific. *Deep-Sea Research Part I: Oceanographic Research Papers*, *62*, 20–31. https://doi.org/10.1016/j.dsr.2011.12.004

Hartin, C. A., Fine, R. A., Sloyan, B. M., Talley, L. D., Chereskin, T. K., & Happell, J. (2011). Formation rates of Subantarctic mode water and Antarctic intermediate water within the South Pacific. *Deep-Sea Research Part I: Oceanographic Research Papers*, *58*(5), 524–534. https://doi.org/10.1016/j.dsr.2011.02.010

Hautala, S. L., & Hammond, D. E. (2020). Abyssal pathways and the Double silica maximum in the northeast Pacific basin. *Geophysical Research Letters*, *47*(19), 1–9. https://doi.org/10.1029/2020GL089010

Hayes, C. T., Black, E. E., Anderson, R. F., Baskaran, M., Buesseler, K. O., Charette, M. A., et al. (2018). Flux of particulate elements in the north Atlantic Ocean constrained by multiple radionuclides. *Global Biogeochemical Cycles*, *32*, 1738–1758. https://doi.org/10.1029/2018GB005994

Hirose, K. (2006). A new method to determine depth-dependent carbon export fluxes using vertical ^{230}Th profiles. *Geophysical Research Letters*, *33*(5), 9–12. https://doi.org/10.1029/2005GL025129

Holzer, M., & Brzezinski, M. A. (2015). Controls on the silicon isotope distribution in the ocean: New diagnostics from a data-constrained model. *Global Biogeochemical Cycles*, *29*(3), 267–287. https://doi.org/10.1002/2014gb004967

Jenkins, W. J., Smethie, W. M., Boyle, E. A., & Cutter, G. A. (2015). Water mass analysis for the U.S. GEOTRACES (GA03) North Atlantic sections. *Deep-Sea Research Part II: Topical Studies in Oceanography*, *116*, 6–20. https://doi.org/10.1016/j.dsr2.2014.11.018

Khatiwala, S., Primeau, F., & Holzer, M. (2012). Ventilation of the deep ocean constrained with tracer observations and implications for radiocarbon estimates of ideal mean age. *Earth and Planetary Science Letters*, *325*(326), 116–125. https://doi.org/10.1016/j.epsl.2012.01.038

Ku, T. L., & Lin, M. C. (1976). ^{226}Ra distribution in the Antarctic Ocean. *Earth and Planetary Science Letters*, *32*(2), 236–248. https://doi.org/10.1016/0012-821X(76)90064-9

Le Roy, E., Sanial, V., Charette, M. A., van Beek, P., Lacan, F., Henderson, P. B., et al. (2018). The ^{226}Ra-Ba relationship in the north Atlantic during GEOTRACES-GA01. *Biogeosciences*, *15*(November), 3027–3048. https://doi.org/10.5194/bg-15-3027-2018

Owens, S. A., Buesseler, K. O., & Sims, K. W. W. (2011). Re-evaluating the 238U-salinity relationship in seawater: Implications for the ^{238}U-^{234}Th disequilibrium method. *Marine Chemistry*, *127*(1–4), 31–39. https://doi.org/10.1016/j.marchem.2011.07.005

Talley, L. D. (2013). Closure of the global overturning circulation through the Indian, Pacific and Southern Oceans: Schematics and transports. *Journal of Chemical Information and Modeling*, *53*(9), 1689–1699. https://doi.org/10.1017/CBO9781107415324.004

Toggweiler, J. R., Dixon, K., & Broecker, W. S. (1991). The Peru upwelling and the ventilation of the south Pacific thermocline. *Journal of Geophysical Research*, *96*(C11), 20467. https://doi.org/10.1029/91jc02063

van Beek, P., François, R., Conte, M., Reyss, J. L., Souhaut, M., & Charette, M. (2007). $^{228}Ra/^{226}Ra$ and $^{226}Ra/Ba$ ratios to track barite formation and transport in the water column. *Geochimica et Cosmochimica Acta*, *71*(1), 71–86. https://doi.org/10.1016/j.gca.2006.07.041

Wolgemuth, K. (1970). Barium analyses from the first Geosecs test cruise. *Journal of Geophysical Research*, *75*(36), 7686–7687. https://doi.org/10.1029/jc075i036p07686